Biogeosciences, 17, 917–943, 2020
https://doi.org/10.5194/bg-17-917-2020

Biogeosciences Open Access EGU

Dissolved iron in the North Atlantic Ocean and Labrador Sea along the GEOVIDE section (GEOTRACES section GA01)

Manon Tonnard[1,2,3], Hélène Planquette[1], Andrew R. Bowie[2,3], Pier van der Merwe[2], Morgane Gallinari[1], Floriane Desprez de Gésincourt[1], Yoan Germain[4], Arthur Gourain[5], Marion Benetti[6,7], Gilles Reverdin[7], Paul Tréguer[1], Julia Boutorh[1], Marie Cheize[1], François Lacan[8], Jan-Lukas Menzel Barraqueta[9,10], Leonardo Pereira-Contreira[11], Rachel Shelley[11,12,13], Pascale Lherminier[14], and Géraldine Sarthou[1]

[1]Univ Brest, CNRS, IRD, Ifremer, LEMAR, 29280 Plouzane, France
[2]Antarctic Climate and Ecosystems – Cooperative Research Centre, University of Tasmania, Hobart, TAS 7001, Australia
[3]Institute for Marine and Antarctic Studies, University of Tasmania, Hobart, TAS 7001, Australia
[4]Laboratoire Cycles Géochimiques et ressources – Ifremer, Plouzané, 29280, France
[5]Ocean Sciences Department, School of Environmental Sciences, University of Liverpool, L69 3GP, UK
[6]Institute of Earth Sciences, University of Iceland, Reykjavik, Iceland
[7]LOCEAN, Sorbonne Universités, UPMC/CNRS/IRD/MNHN, Paris, France
[8]LEGOS, Université de Toulouse – CNRS/IRD/CNES/UPS – Observatoire Midi-Pyrénées, Toulouse, France
[9]GEOMAR Helmholtz-Zentrum für Ozeanforschung Kiel Wischhofstraße 1–3, Geb. 12, 24148 Kiel, Germany
[10]Department of Earth Sciences, Stellenbosch University, Stellenbosch, 7600, South Africa
[11]Fundação Universidade Federal do Rio Grande (FURG), R. Luis Loréa, Rio Grande – RS, 96200-350, Brazil
[12]Dept. of Earth, Ocean and Atmospheric Science, Florida State University, 117 N Woodward Ave, Tallahassee, Florida 32301, USA
[13]School of Geography, Earth and Environmental Sciences, University of Plymouth, Drake Circus, Plymouth, PL4 8AA, UK
[14]Ifremer, Univ Brest, CNRS, IRD, Laboratoire d'Océanographie Physique et Spatiale (LOPS), IUEM, 29280, Plouzané, France

Correspondence: Géraldine Sarthou (geraldine.sarthou@univ-brest.fr) and Hélène Planquette (helene.planquette@univ-brest.fr)

Received: 26 March 2018 – Discussion started: 4 April 2018
Revised: 2 December 2019 – Accepted: 9 January 2020 – Published: 21 February 2020

Abstract. Dissolved Fe (DFe) samples from the GEOVIDE voyage (GEOTRACES GA01, May–June 2014) in the North Atlantic Ocean were analyzed using a sea*FAST*-pico™ coupled to an Element XR sector field inductively coupled plasma mass spectrometer (SF-ICP-MS) and provided interesting insights into the Fe sources in this area. Overall, DFe concentrations ranged from 0.09 ± 0.01 to 7.8 ± 0.5 nmol L^{-1}. Elevated DFe concentrations were observed above the Iberian, Greenland, and Newfoundland margins likely due to riverine inputs from the Tagus River, meteoric water inputs, and sedimentary inputs. Deep winter convection occurring the previous winter provided iron-to-nitrate ratios sufficient to sustain phytoplankton growth and lead to relatively elevated DFe concentrations within subsurface waters of the Irminger Sea. Increasing DFe concentrations along the flow path of the Labrador Sea Water were attributed to sedimentary inputs from the Newfoundland Margin. Bottom waters from the Irminger Sea displayed high DFe concentrations likely due to the dissolution of Fe-rich particles in the Denmark Strait Overflow Water and the Polar Intermediate Water. Finally, the nepheloid layers located in the different basins and at the Iberian Margin were found to act as either a source or a sink of DFe depending on the nature of particles,

Published by Copernicus Publications on behalf of the European Geosciences Union.

with organic particles likely releasing DFe and Mn particle scavenging DFe.

1 Introduction

The North Atlantic Ocean is known for its pronounced spring phytoplankton blooms (Henson et al., 2009; Longhurst, 2007). Phytoplankton blooms induce the capture of aqueous carbon dioxide through photosynthesis, and conversion into particulate organic carbon (POC). This POC is then exported into deeper waters through sinking and ocean currents. Via these processes, and in conjunction with the physical carbon pump, the North Atlantic Ocean is the largest oceanic sink of anthropogenic CO_2 (Pérez et al., 2013), despite covering only 15 % of global ocean area (Humphreys et al., 2016; Sabine et al., 2004), and is therefore crucial for Earth's climate.

Indeed, phytoplankton must obtain, besides light and inorganic carbon, chemical forms of essential elements termed nutrients to be able to photosynthesize. The availability of these nutrients in the upper ocean frequently limits the activity and abundance of these organisms together with light conditions (Moore et al., 2013). In particular, winter nutrient reserves in surface waters set an upper limit for biomass accumulation during the annual spring-to-summer bloom and will influence the duration of the bloom (Follows and Dutkiewicz, 2001; Henson et al., 2009; Moore et al., 2013, 2008). Hence, nutrient depletion due to biological consumption is considered a major factor in the decline of blooms (Harrison et al., 2013).

The extensive studies conducted in the North Atlantic Ocean through the continuous plankton recorder (CPR) have highlighted the relationship between the strength of the westerlies and the displacement of the subarctic front (SAF), (which corresponds to the North Atlantic Oscillation (NAO) index; Bersch et al., 2007) and the phytoplankton dynamics of the central North Atlantic Ocean (Barton et al., 2003). Therefore, the SAF delineates the subtropical gyre from not only the subpolar gyre but also two distinct systems in which phytoplankton limitations are controlled by different factors. In the North Atlantic Ocean, spring phytoplankton growth is largely light limited within the subpolar gyre. Light levels are primarily set by freeze–thaw cycles of sea ice and the high-latitude extremes in the solar cycle (Longhurst, 2007). Simultaneously, intense winter mixing supplies surface waters with high concentrations of nutrients. In contrast, within the subtropical gyre, the spring phytoplankton growth is less impacted by the light regime and has been shown to be N and P co-limited (e.g., Harrison et al., 2013; Moore et al., 2008). This is principally driven by Ekman downwelling with an associated export of nutrients out of the euphotic zone (Oschlies, 2002). Thus, depending on the location of the SAF, phytoplankton communities from the central North Atlantic Ocean will be primarily light or nutrient limited.

However, once the water column stratifies and phytoplankton are released from light limitation, seasonal high-nutrient, low-chlorophyll (HNLC) conditions were reported at the transition zone between the gyres, especially in the Irminger Sea and Iceland Basin (Sanders et al., 2005). In these HNLC zones, trace metals are most likely limiting the biological carbon pump. Among all the trace metals, Fe has been recognized as the prime limiting element of North Atlantic primary productivity (e.g., Boyd et al., 2000; Martin et al., 1994, 1988, 1990). Indeed, Fe is a key element for a number of metabolic processes (e.g., Morel et al., 2008). However, the phytoplankton community has been shown to become N and/or Fe-(co)-limited in the Iceland Basin and the Irminger Sea (e.g., Nielsdóttir et al., 2009; Painter et al., 2014; Sanders et al., 2005).

In the North Atlantic Ocean, dissolved Fe (DFe) is delivered through multiple pathways such as ice melting (e.g., Klunder et al., 2012; Tovar-Sanchez et al., 2010), atmospheric inputs (Achterberg et al., 2018; Baker et al., 2013; Shelley et al., 2015, 2017), coastal runoff (Rijkenberg et al., 2014), sediment inputs (Hatta et al., 2015), hydrothermal inputs (Achterberg et al., 2018; Conway and John, 2014), and water mass circulation (vertical and lateral advections; e.g., Laës et al., 2003). Dissolved Fe can be regenerated through biological recycling (microbial loop, zooplankton grazing; e.g., Boyd et al., 2010; Sarthou et al., 2008). Iron is removed from the dissolved phase by biological uptake, export, and scavenging throughout the water column and precipitation (itself a function of salinity, pH of seawater, and ligand concentrations).

Although many studies investigated the distribution of DFe in the North Atlantic Ocean, much of this work was restricted to the upper layers (< 1000 m depth) or to one basin. Therefore, uncertainties remain on the large-scale distribution of DFe in the North Atlantic Ocean and more specifically within the subpolar gyre where few studies have been undertaken, and even fewer in the Labrador Sea. In this biogeochemically important area, high-resolution studies are still lacking understanding of the processes influencing the cycle of DFe.

The aim of this paper is to elucidate the sources and sinks of DFe and its distribution regarding water masses and to assess the links with biological activity along the GEOVIDE (GEOTRACES-GA01) transect. This transect spans several biogeochemical provinces including the West European Basin, the Iceland Basin, and the Irminger and the Labrador seas (Fig. 1). In doing so we hope to constrain the potential long-range transport of DFe through the Deep Western Boundary Current (DWBC) via the investigation of the local processes effecting the DFe concentrations within the three main water masses that constitute it: Iceland–Scotland Overflow Water (ISOW), Denmark Strait Overflow Water (DSOW), and Labrador Sea Water (LSW).

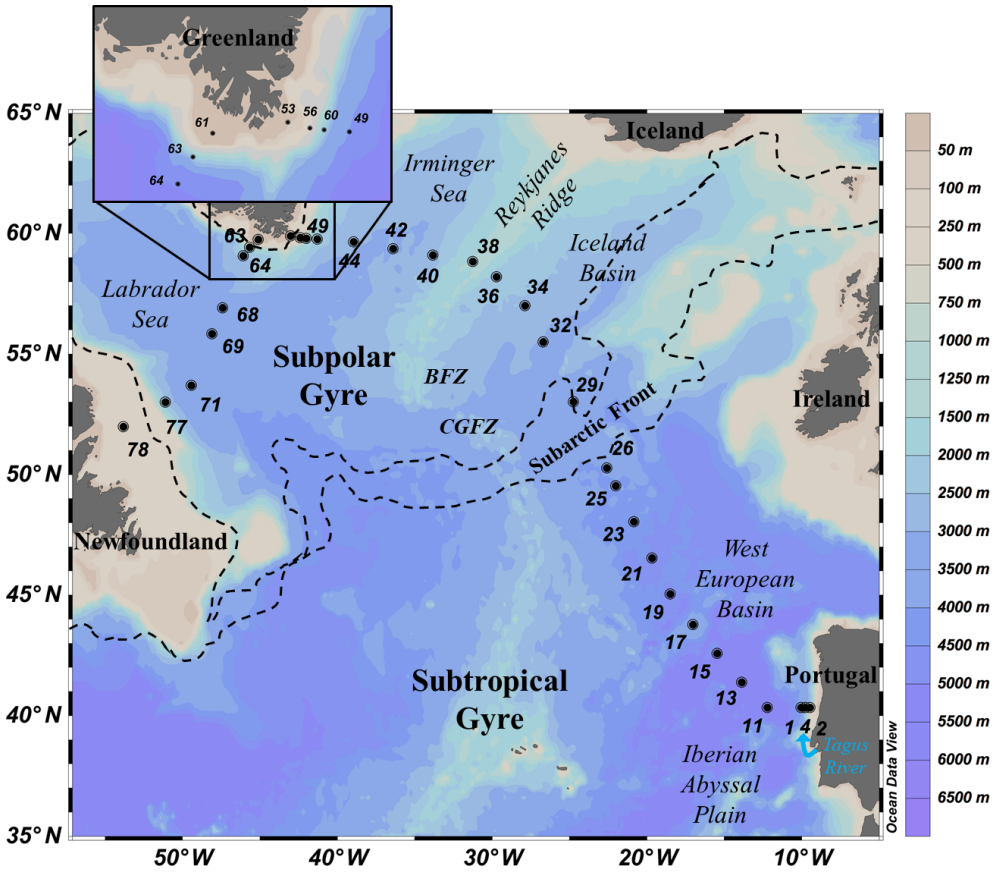

Figure 1. Map of the GEOTRACES GA01 voyage plotted on bathymetry as well as the major topographical features and main basins (Ocean Data View (ODV) software, version 4.7.6, Schlitzer, 2016; http://odv.awi.de, last access: 30 January 2020). BFZ: Bight Fracture Zone; CGFZ: Charlie-Gibbs Fracture Zone.

2 Material and methods

2.1 Study area and sampling activities

Samples were collected during the GEOVIDE (GEOTRACES-GA01 section, Fig. 1) oceanographic voyage from 15 May 2014 (Lisbon, Portugal) to 30 June 2014 (St. John's, Newfoundland, Canada) aboard N/O *Pourquoi Pas?*. The study was carried out along the OVIDE line (http://www.umr-lops.fr/Projets/Projets-actifs/OVIDE, last access: 30 January 2020, previously referred to as the WOCE A25 Greenland-to-Portugal section) and in the Labrador Sea (corresponding to the WOCE A01 leg 3 Greenland-to-Newfoundland section). The OVIDE line has been sampled every 2 years since 2002 in the North Atlantic (e.g., Mercier et al., 2015) and in the Labrador Sea (broadly corresponding to the WOCE A01 leg 3 Greenland-to-Newfoundland section). In total, 32 stations were occupied, and samples were usually collected at 22 depths, except at shallower stations close to the Iberian, Greenland, and Canadian shelves (Fig. 1) where fewer samples (between 6 and 11) were collected. To avoid ship contamination of surface waters, the shallowest sampling depth was 15 m at all stations. Therefore, "surface water samples" refers to 15 m depth.

Samples were collected using a trace metal clean polyurethane powder-coated aluminum frame rosette (hereafter referred to as TMR) equipped with twenty-two 12 L, externally closing, Teflon-lined GO-FLO bottles (General Oceanics) and attached to a Kevlar® line. The cleaning protocols for sampling bottles and equipment followed the guidelines of the GEOTRACES Cookbook (http://www.geotraces.org, last access: 30 January 2020, Cutter et al., 2017). After TMR recovery, GO-FLO bottles were transferred into a clean container equipped with a class 100 laminar flow hood. Samples were either taken from the filtrate of particulate samples (collected on polyethersulfone filters, 0.45 µm supor®; see Gourain et al., 2019) or after filtration using 0.2 µm filter cartridges (Sartorius Sartobran® 300) due to water budget restriction (Table 1). Filtration techniques were not directly compared for the same samples; however, Wilcoxon statistical tests were performed to compare the distribution of DFe at each pair of adjacent stations where the change of filtration technique was performed (see Table 1). No significant

differences were observed (p value > 0.2) for all pairs of stations ($n = 9$), except between stations 11 and 13 and between stations 13 and 15. Moreover, both filtration techniques are deemed acceptable by the GEOTRACES guidelines. Seawater was collected in acid-cleaned 60 mL LDPE bottles, after rinsing three times with about 20 mL of seawater. Teflon® tubing used to connect the filter holders or cartridges to the GO-FLO bottles was washed in an acid bath (10 % v/v HCl, Suprapur®, Merck) for at least 12 h and rinsed three times with ultra-high-purity water (UHPW > 18 MΩ cm) prior to use. Samples were then acidified to ∼ pH 1.7 with HCl (Ultrapur® Merck, 2 ‰ v/v) under a class 100 laminar flow hood inside the clean container. The sample bottles were then double bagged and stored at ambient temperature in the dark before shore-based analyses 1 year after collection.

Large volumes of seawater sample (referred to hereafter as the in-house standard seawater) were also collected using a towed fish at around 2–3 m deep and filtered in-line inside a clean container through a 0.2 µm pore size filter capsule (Sartorius SARTOBRAN® 300) and stored unacidified in 20–30 L LDPE carboys (Nalgene™). All the carboys were cleaned following the guidelines of the GEOTRACES Cookbook (Cutter et al., 2017). This in-house standard seawater was used for calibration on the sea*FAST*-pico™ SF-ICP-MS (see Sect. 2.2) and was acidified to ∼ pH 1.7 with HCl (Ultrapur® Merck, 2 ‰ v/v) at least 24 h prior to analysis.

2.2 DFe analysis with sea*FAST*-pico™

Seawater samples were preconcentrated using a sea*FAST*-pico™ (ESI, Elemental Scientific, USA) and the eluent was directly introduced via a perfluoroalkoxy alkane screw-thread (PFA-ST) nebulizer and a cyclonic spray chamber in an Element XR sector field inductively coupled plasma mass spectrometer (Element XR SF-ICP-MS, Thermo Fisher Scientific Inc., Omaha, NE), following the protocol of Lagerström et al. (2013).

High-purity-grade solutions and water (Milli-Q) were used to prepare the following reagents each day: the acetic acid–ammonium acetate buffer (CH_3COO^- and NH_4^+) was made of 140 mL acetic acid (>99 % NORMATOM® – VWR Chemicals) and ammonium hydroxide (25 %, Merck Suprapur®) in 500 mL PTFE bottles and was adjusted to pH 6.0 ± 0.2 for the on-line pH adjustment of the samples. The eluent was made of 1.4 M nitric acid (HNO_3, Merck Ultrapur®) in Milli-Q water by a 10-fold dilution and spiked with 1 µg L^{-1} ^{115}In (SCP Science calibration standards) to allow for drift correction. Autosampler and column rinsing solutions were made of HNO_3 2.5 % (v/v) (Merck Suprapur®) in Milli-Q water. The carrier solution driven by the syringe pumps to move the sample and buffer through the flow injection system was made in the same way.

All reagents, standards, samples, and blanks were prepared in acid-cleaned low-density polyethylene (LDPE) or Teflon fluorinated ethylene propylene (FEP) bottles. Bottles were cleaned following the GEOTRACES protocol (Cutter et al., 2017).

Mixed-element standard solution was prepared gravimetrically using high-purity standards (Fe, Mn, Cd, Co, Zn, Cu, Pb; SCP Science calibration standards) in HNO_3 3 % (v/v) (Merck Ultrapur®). The distribution of the trace metals other than Fe will be reported elsewhere (Planquette et al., 2020). A six-point calibration curve was prepared by standard additions of the mixed element standard to our acidified in-house standard and ran at the beginning, the middle, and the end of each analytical session. Each analytical session consisted of about 50 samples. Final concentrations of samples and procedural blanks were calculated from In-normalized data. Data were blank-corrected by subtracting an average acidified Milli-Q blank that was preconcentrated on the sea*FAST*-pico™ in the same way as the samples and seawater standards. The errors associated with each sample were calculated as the standard deviation for five measurements of low-Fe seawater samples. The mean Milli-Q blank was equal to 0.08 ± 0.09 nmol L^{-1} ($n = 17$) considering all analytical sessions. The detection limit, calculated for a given run as 3 times the standard deviation of the Milli-Q blanks, was on average 0.05 ± 0.05 nmol L^{-1} ($n = 17$). Reproducibility was assessed through the standard deviation of replicate samples (every 10th sample was a replicate) and the average of the in-house standard seawater and was equal to 17 % ($n = 84$). Accuracy was determined from the analysis of consensus (SAFe S, GSP) and certified (NASS-7) seawater matrices (see Table 2) and in-house standard seawater (DFe $= 0.42 \pm 0.07$ nmol L^{-1}, $n = 84$). Note that all the DFe values were generated in nanomoles per kilogram using the sea*FAST*-pico™ coupled to an Element XR SF-ICP-MS and were converted to nanomoles per liter using the actual density (kg L^{-1}) of each seawater sample (Table 1) to be directly comparable with literature.

2.3 Meteoric water and sea ice fraction calculation

We considered the different contributions of sea ice melt (SIM), meteoric water (MW), and saline seawater, at Stations 53, 61, and 78 using the procedure and mass balance calculations that are fully described in Benetti et al. (2016). Briefly, we considered two types of seawater, namely Atlantic Water (AW) and Pacific Water (PW). The relative proportions of AW (f_{AW}) and PW (f_{PW}) are calculated based on the distinctive nitrogen-to-phosphorus (N–P) relationships for the two water masses (Jones et al., 1998) as follows (e.g., Sutherland et al., 2009):

$$f_{PW} = \frac{N^m - N^{AW}}{N^{PW} - N^{AW}}, \quad (1)$$

where N^m is the measured dissolved inorganic nitrogen, and N^{AW} and N^{PW} are the values for pure Atlantic and Pacific water, respectively, estimated from Jones et al. (1998), and N^{AW} and N^{PW} values are calculated by substituting the

Table 1. Station number, date of sampling (in the dd/mm/yyyy format), pore size used for filtration (µm), station location, mixed-layer depth (m), and associated average dissolved iron (DFe) concentrations, standard deviation, and number of samples during the GEOTRACES GA01 transect. Note that the asterisk next to station numbers refers to disturbed temperature and salinity profiles as opposed to uniform profiles.

Station	Date sampling (dd/mm/yyyy)	Filtration (µm)	Latitude (° N)	Longitude (° E)	Z_m (m)	DFe (nmol L^{-1}) average SD	n
1	19/05/2014	0.2	40.33	−10.04	25.8	1.07 ± 0.12	1
2	21/05/2014	0.2	40.33	−9.46	22.5	1.01 ± 0.04	1
4	21/05/2014	0.2	40.33	−9.77	24.2	0.73 ± 0.03	1
11	23/05/2014	0.2	40.33	−12.22	31.3	0.20 ± 0.11	2
13	24/05/2014	0.45	41.38	−13.89	18.8	0.23 ± 0.02	1
15	28/05/2014	0.2	42.58	−15.46	34.2	0.22 ± 0.03	2
17	29/05/2014	0.2	43.78	−17.03	36.2	0.17 ± 0.01	1
19*	30/05/2014	0.45	45.05	−18.51	44.0	0.13 ± 0.05	2
21	31/05/2014	0.2	46.54	−19.67	47.4	0.23 ± 0.08	2
23*	02/06/2014	0.2	48.04	−20.85	69.5	0.21 ± 0.05	6
25	03/06/2014	0.2	49.53	−22.02	34.3	0.17 ± 0.04	2
26	04/06/2014	0.45	50.28	−22.60	43.8	0.17 ± 0.03	2
29	06/06/2014	0.45	53.02	−24.75	23.8	0.17 ± 0.02	1
32	07/06/2014	0.2	55.51	−26.71	34.8	0.59 ± 0.08	2
34	09/06/2014	0.45	57.00	−27.88	25.6	NA	0
36	10/06/2014	0.45	58.21	−29.72	33.0	0.12 ± 0.02	1
38	10/06/2014	0.45	58.84	−31.27	34.5	0.36 ± 0.16	2
40	12/06/2014	0.45	59.10	−33.83	34.3	0.39 ± 0.05	1
42	12/06/2014	0.45	59.36	−36.40	29.6	0.36 ± 0.05	1
44	13/06/2014	0.2	59.62	−38.95	25.8	NA	0
49	15/06/2014	0.45	59.77	−41.30	60.3	0.30 ± 0.05	2
53*	17/06/2014	0.45	59.90	−43.00	36.4	NA	0
56*	17/06/2014	0.45	59.82	−42.40	30.0	0.87 ± 0.06	1
60*	17/06/2014	0.45	59.80	−42.00	36.6	0.24 ± 0.02	2
61*	19/06/2014	0.45	59.75	−45.11	39.8	0.79 ± 0.12	1
63*	19/06/2014	0.45	59.43	−45.67	86.7	0.40 ± 0.03	1
64	20/06/2014	0.45	59.07	−46.09	33.9	0.27 ± 0.06	2
68*	21/06/2014	0.45	56.91	−47.42	26.3	0.22 ± 0.01	1
69*	22/06/2014	0.45	55.84	−48.09	17.5	0.24 ± 0.02	1
71	24/06/2014	0.45	53.69	−49.43	36.7	0.32 ± 0.04	2
77*	26/06/2014	0.45	53.00	−51.10	26.1	NA	0
78	27/06/2014	0.45	51.99	−53.82	13.4	0.79 ± 0.05	1

NA: not available.

PO_4^m value in the equation of the pure AW and PW N–P lines from Jones et al. (1998). However, during GEOVIDE, the phosphate-depleted near-surface values led to unrealistic lower N^{PW} than just below the subsurface. Therefore, for all surface samples, the N^{PW} was replaced by the values at 100 m. Then, the surface values were adjusted by a factor of dilution proportional to the sample salinity.

After estimating f_{AW} and f_{PW} and their respective salinity and $\delta^{18}O$ affecting each sample, the contribution of SIM and MW can be determined using measured salinity (S_m) and $\delta^{18}O$ (δO_m^{18}). The mass balance calculations are presented below:

$$f_{AW} + f_{PW} + f_{MW} + f_{SIM} = 1, \quad (2)$$

$$f_{AW}S_{AW} + f_{PW}S_{PW} + f_{MW}S_{MW} + f_{SIM}S_{SIM} = S_m, \quad (3)$$

$$f_{AW}\delta O_{AW}^{18} + f_{PW}\delta O_{PW}^{18} + f_{MW}\delta O_{MW}^{18} + f_{SIM}\delta O_{SIM}^{18} = \delta O_m^{18}, \quad (4)$$

where f_{AW}, f_{PW}, f_{MW}, and f_{SIM} are the relative fraction of AW, PW, MW, and SIM. To calculate the relative fractions of AW, PW, MW, and SIM, we used the following end-members: $S_{AW} = 35$, $\delta O_{AW}^{18} = +0.18$ ‰ (Benetti et al., 2016); $S_{PW} = 32.5$, $\delta O_{PW}^{18} = -1$ ‰ (Cooper et al., 1997; Woodgate and Aagaard, 2005); $S_{MW} = 0$, $\delta O_{MW}^{18} = -18.4$ ‰ (Cooper et al., 2008); $S_{SIM} = 4$, $\delta O_{SIM}^{18} = +0.5$ ‰ (Melling and Moore, 1995).

Table 2. SAFe S, GSP, and NASS-7 dissolved iron concentrations (DFe, nmol L-1) determined by the sea*FAST*-pico™ instruments and their consensus (SAFe S, GSP; https://websites.pmc.ucsc.edu/~kbruland/GeotracesSaFe/kwbGeotracesSaFe.html, last access: 30 January 2020) and certified (NASS-7; https://www.nrc-cnrc.gc.ca/eng/solutions/advisory/crm/certificates/nass_7.html, last access: 30 January 2020) DFe concentrations. Note that no consensual value is reported for the GSP seawater.

	DFe values ($nmol\,L^{-1}$)		
	Sea *FAST*-pico™		Reference or certified
Seawater used	Average (±SD)	n	Average (±SD)
SAFe S	0.100 (±0.006)	2	0.095 (±0.008)
GSP	0.16 (±0.04)	15	0.155 (±0.05)
NASS-7	6.7 (±1.7)	12	6.3 (±0.5)

Negative sea ice fractions indicated a net brine release while positive sea ice fractions indicated a net sea ice melting. Note that for stations over the Greenland Shelf, we assumed that the Pacific Water (PW) contribution was negligible for the calculations, supported by the very low PW fractions found at Cape Farewell in May 2014 (see Fig. B1 in Benetti et al., 2017), while for station 78, located on the Newfoundland shelf, we used nutrient measurements to calculate the PW fractions, following the approach from Jones et al. (1998) (the data are published in Benetti et al., 2017).

2.4 Ancillary measurements and mixed-layer depth determination

Potential temperature (θ), salinity (S), dissolved oxygen (O_2), and beam attenuation data were retrieved from the conductivity–temperature–depth (CTD) sensors (CTD SBE911 equipped with a SBE-43) that were deployed on a stainless-steel rosette. Salinity profiles were calibrated using 1228 samples taken from the GO-FLO bottles, leading to a precision of 0.002 psu. The O_2 data could not be directly calibrated with GO-FLO samples, due to the sampling time being too long, so the calibrated O_2 profiles acquired by the classic CTD at the same station were used to calibrate the O_2 profiles of the TMR CTD, with a precision estimated at $3\,\mu mol\,kg^{-1}$. Nutrient and total chlorophyll a (TChl a) samples were collected using the classic CTD at the same stations as for the TMR. We used the data from the stainless-steel rosette casts that were deployed immediately before or after our TMR casts. Pigments were separated and quantified following an adaptation of the method described by Van Heukelem and Thomas (2001) and the analytical procedure used is described in Ras et al. (2008). The method adaptation allowed for higher sensitivity in the analysis of low-phytoplankton-biomass waters (see Ras et al., 2008). Briefly, frozen filters were extracted at −20 °C in 3 mL of methanol (100 %), sonicated, and then clarified by vacuum filtration through Whatman GF/F filters. The total extraction time was 2 h. The extracts were then analyzed by HPLC with a complete Agilent Technologies 1200 system (comprising LC ChemStation software, a degasser, a binary pump, a refrigerated autosampler, a column thermostat, and a diode array detector) when possible on the same day as extraction. The sample extracts were premixed (1 : 1) with a tetrabutylammonium acetate (TBAA) buffer solution (28 nM) prior to injection in the HPLC. The mobile phase was a mix between a solution (a) of TBAA 28 mM / methanol (30/70, v/v) and a solution (b) of 100 % methanol (i.e., the organic solvent) with varying proportions during analysis. After elution, pigment concentrations ($mg\,m^{-3}$) were calculated according to Beer–Lambert's law (i.e., $A = \varepsilon LC$) from the peak areas with an internal standard correction (vitamin E acetate, Sigma) and an external standard calibration (DHI Water and Environment, Denmark). This method allowed the detection of 23 phytoplankton pigments. The detection limits, defined as 3 times the signal : noise ratio for a filtered volume of 1 L, was $0.0001\,mg\,m^{-3}$ for total chlorophyll a (TChl a), and its injection precision was 0.91 %

All these data are available on the LEFE CYBER database (http://www.obs-vlfr.fr/proof/php/geovide/geovide.php, last access: 30 January 2020).

The mixed-layer depth (Z_m) for each station was calculated using the function "calculate.mld" (part of the "rcalcofi" package, Ed Weber at NOAA SWFSC) created by Sam McClathie (NOAA Federal, 30 December 2013) for R software and where Z_m is defined as an absolute change in the density of seawater at a given temperature ($\Delta\sigma_\theta \geq 0.125\,kg\,m^{-3}$) with respect to an approximately uniform region of density just below the ocean surface (Kara et al., 2000). In addition to the density criterion, the temperature and salinity profiles were inspected at each station for uniformity within this layer. When they were not uniform, the depth of any perturbation in the profile was chosen as the base of the Z_m (Table 1).

2.5 Statistical analysis

All statistical approaches, namely the comparison between the pore size used for filtration, correlations, and principal component analysis (PCA), were performed using the R statistical software (R development Core Team, 2012). For all the results, p values were calculated against the threshold value alpha (α), which we assigned at 0.05, corresponding to a 95 % level of confidence. For all datasets, non-normal distributions were observed according to the Shapiro–Wilk test. Therefore, the significance level was determined with a Wilcoxon test.

All sections and surface layer plots were prepared using Ocean Data View (Schlitzer, 2016).

2.6 Water mass determination and associated DFe concentrations

The water mass structure in the North Atlantic Ocean from the GEOVIDE voyage was quantitatively assessed by means of an extended optimum multiparameter (eOMP) analysis with 14 water masses (for details see García-Ibáñez et al., 2015; this issue). Using this water mass determination, DFe concentrations were considered representative of a specific water mass only when the contribution of this specific water mass was higher than 60 % of the total water mass pool.

2.7 Database

The complete database of dissolved Fe is available in the electronic supplement (http://www.biogeosciences.net). Overall, 540 data points of dissolved Fe are reported, among which 511 values are used in this paper. The remaining 29 values (5.7 % of the total dataset) are flagged as (suspect) outliers. These 29 outliers, flagged as "3" in the table, were not used in figures or in the interpretation of this paper. The criteria for rejection were based on the comparison with other parameters measured from the same GO-FLO sampler and curve fitting versus samples collected above and below the suspect sample. The complete dataset will be available in national and international databases (LEFE CYBER, http://www.obs-vlfr.fr/proof/index2.php, last access: 30 January 2020, and GEOTRACES http://www.bodc.ac.uk/geotraces/, last access: 30 January 2020).

3 Results

3.1 Hydrography

The hydrology and circulation of the main water masses along the OVIDE section in the North Atlantic Subpolar Gyre and their contribution to the Atlantic Meridional Overturning Circulation (AMOC) have been described using an eOMP analysis by García-Ibáñez et al. (2015, 2018) and Zunino et al. (2017). For a schematic of water masses, currents, and pathways, see Daniault et al. (2016). Hereafter we summarize the main features (Figs. 1 and 2).

Upper waters (∼ 0–800 m). The cyclonic circulation of Eastern North Atlantic Central Water (ENACW) ($12.3<\theta<16\,^{\circ}C$, $35.66<S<36.2$, $241<O_2<251\,\mu mol\,kg^{-1}$) occupied the water column from 0 to ∼ 800 m depth from stations 1 to 25 representing 60 % of the water mass pool. The sharp Subarctic Front (between stations 26 and 29), caused by the northern branch of the North Atlantic Current (NAC) separated the cyclonic subpolar from the anticyclonic subtropical gyre domains at 50° N and 22.5° W. ENACW were also encountered to a lesser extent and only in surface waters (from 0 to ∼ 100 m depth) between stations 29 and 34 (representing less than 40 % of the water mass pool). West of the Subarctic Front, Iceland Subpolar Mode Water (IcSPMW, $7.07<\theta<8\,^{\circ}C$, $35.16<S<35.23$, $280<O_2<289\,\mu mol\,kg^{-1}$) was encountered from stations 34–40 (accounting for more than 45 % of the water mass pool from 0 to ∼ 800 m depth) and Irminger Subpolar Mode Water (IrSPMW, $\theta \approx 5\,^{\circ}C$, $S \approx 35.014$) from stations 42–44 (representing to 40 % of the water mass pool from 0 to ∼ 250 m depth) and stations 49 and 60 (accounting for 40 % of the water mass pool down to 1300 m depth). IcSPMW was also observed within the subtropical gyre (stations 11–26), subducted below ENACW up to 1000 m depth. Stations 63 (> ∼ 200 m depth) and 64 (from surface down to ∼ 500 m depth) exhibited a contribution of the IrSPMW higher than 45 %. Stations 44, 49 and 60, from the Irminger Sea, and 63 from the Labrador Sea were characterized by lower sea-surface salinity ranges ($S = [34.636, 34.903]$, stations 63 and 60, respectively), likely due to ice melting and meteoric water inputs. Subarctic Intermediate Water (SAIW, $4.5<\theta<6.0\,^{\circ}C$, $34.70<S<34.80$) contributed to more than 40 % of the water mass pool in the Iceland Basin between the surface and ∼ 400 m depth at stations 29 and 32 and throughout the water column of stations 53, 56 and 61 and from surface down to ∼ 200 m depth at station 63. From stations 68 to 78 surface waters were characterized by a minimum of salinity and a maximum of oxygen ($S = 34.91$, $O_2 = 285\,\mu mol\,kg^{-1}$, $\theta \approx 3\,^{\circ}C$) and corresponded to the newly formed Labrador Sea Water (LSW). The LSW was also observed in surface waters of station 44 with a similar contribution than IrSPMW (∼ 40 %).

Intermediate waters (∼ 800–1400 m). Mediterranean Outflow Water (MOW), distinguishable from surrounding Atlantic Water by its high salinity tongue (up to 36.2), a minimum of oxygen ($O_2 = 210\,\mu mol\,kg^{-1}$) and relatively high temperatures (up to 11.7 °C) was observed from station 1 to 21 between 800 and 1400 m depth at a neutral density ranging from 27.544 to $27.751\,kg\,m^{-3}$ with the maximum contribution to the whole water mass pool seen at station 1 (64 ± 6 %). Its main core was located at ∼ 1200 m depth off the Iberian shelf from stations 1 to 11 and then gradually rising westward due to mixing with LSW within the North Atlantic subtropical gyre and a contribution of this water mass decreasing until station 21 down to 10 %–20 %. LSW ($27.763 <$ neutral density $< 27.724\,kg\,m^{-3}$) was sourced from Subpolar Mode waters (SPMW) after intense heat loss and led to its deep convection. During GEOVIDE, LSW formed by deep convection the previous winter was found at several stations in the Labrador Sea (68, 69, 71 and 77). After convecting, LSW splits into three main branches with two main cores separated by the Reykjanes Ridge (stations 1–32, West European and Iceland basins; stations 40–60, Irminger Sea), and the last one entering the West European Basin (Zunino et al., 2017).

Overflows and deep waters (∼ 1400–5500 m). North East Atlantic Deep Water (NEADW, $1.98<\theta<2.50\,^{\circ}C$, $34.895<S<34.940$) was the dominant water mass in the West European Basin at stations 1–29 from 2000 m depth

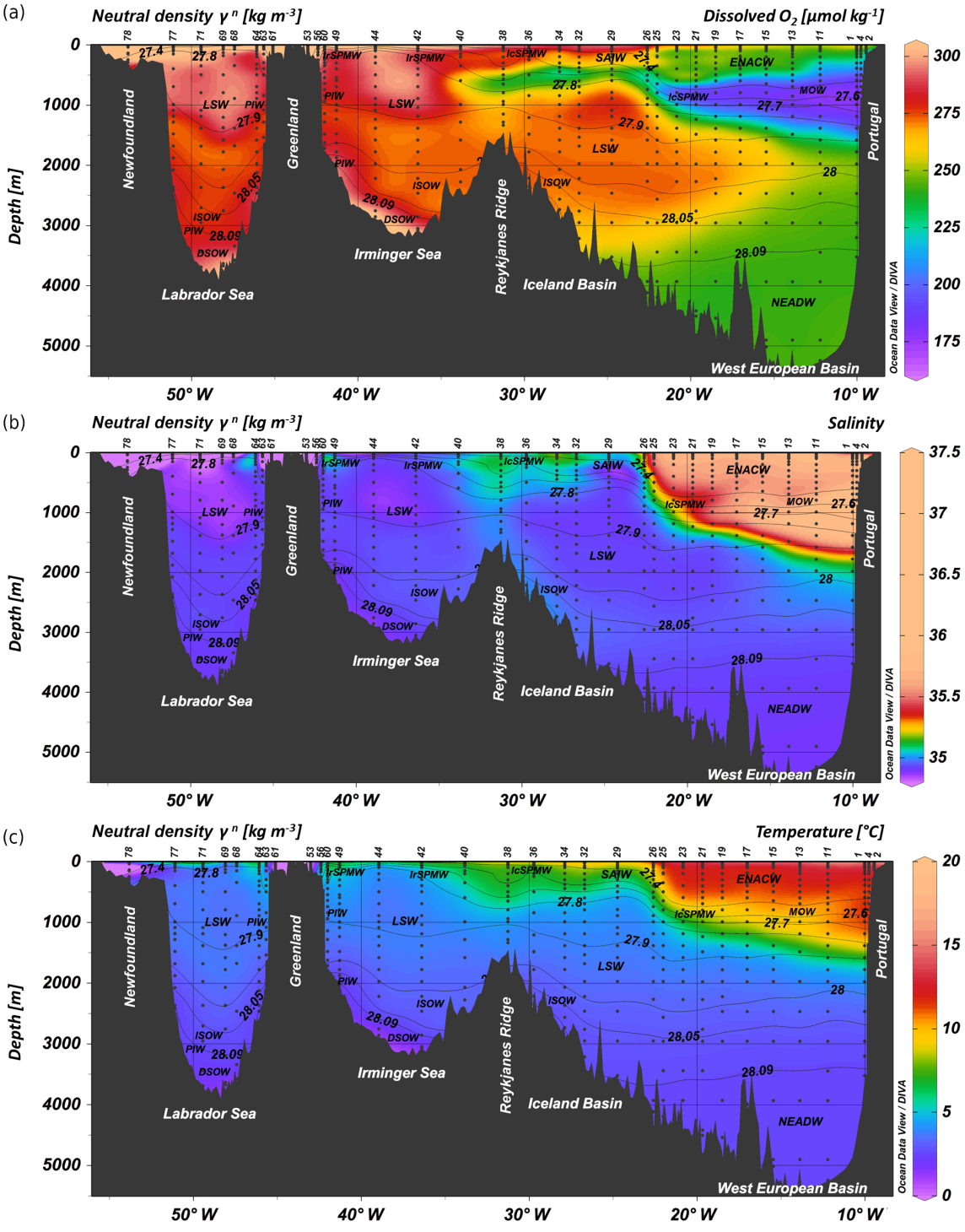

Surface water masses

ENACW	East North Atlantic Central Water
IcSPMW	Iceland SubPolar Mode Water
IrSPMW	Irminger SubPolar Mode Water
SAIW	Subarctic Intermediate Water

Intermediate water masses

MOW	Mediterranean Outflow Water
LSW	Labrador Sea Water

Overflow deep water masses

NEADW	North East Atlantic Deep Water
PIW	Polar Intermediate Water
ISOW	Iceland-Scotland Overflow Water
DSOW	Denmark Strait Overflow Water

Currents

NAC	North Atlantic Current
EGC	East Greenland Current
EGCC	East Greenland Coastal Current
WGC	West Greenland Current
LC	Labrador Current

Figure 2. Parameters measured from the regular CTD cast represented as a function of depth for the GA01 section for **(a)** dissolved oxygen (O_2, µmol kg^{-1}), **(b)** salinity, and **(c)** temperature (°C). The contour lines represent isopycnals (neutral density, γ^n, in units of kilogram per cubic meter) (Ocean Data View (ODV) software, version 4.7.6, Schlitzer, 2016; http://odv.awi.de, last access: 30 January 2020).

to the bottom and is characterized by high silicic acid ($42 \pm 4\,\mu mol\,L^{-1}$), nitrate ($21.9 \pm 1.5\,\mu mol\,L^{-1}$) concentrations and lower oxygen concentration ($O_2 \approx 252\,\mu mol\,kg^{-1}$) (see Sarthou et al., 2018). The core of the NEADW (stations 1–13) was located near the seafloor and gradually decreased westward. Polar Intermediate Water (PIW, $\theta \approx 0\,°C$, $S \approx 34.65$) is a ventilated, dense, low-salinity water intrusion to the deep overflows within the Irminger and Labrador seas that is formed at the Greenland shelf. PIW represents only a small contribution to the whole water mass pool (up to 27 %) and was observed over the Greenland slope at stations 53 and 61 as well as in surface waters from station 63 (from 0 to ~ 200 m depth), in intermediate waters of stations 49, 60, and 63 (from ~ 500 to ~ 1500 m depth) and in bottom waters of stations 44, 68, 69, 71, and 77 with a contribution higher than 10 %. Iceland–Scotland Overflow Water (ISOW, $\theta \approx 2.6\,°C$, $S \approx 34.98$) is partly formed within the Arctic Ocean by convection of the modified Atlantic water. ISOW comes from the Iceland–Scotland sills and flows southward towards the Charlie-Gibbs Fracture Zone (CGFZ) and Bight Fracture Zone (BFZ) (stations 34 and 36), after which it reverses its flowing path northward and enters the Irminger Sea (stations 40 and 42) to finally reach the Labrador Sea close to the Greenland coast (station 49, station 44 being located in between these two opposite flow paths). Along the eastern (stations 26–36) and western (stations 40–44) flanks of the Reykjanes Ridge, ISOW had a contribution higher than 50 % to the water mass pool. ISOW was observed from 1500 m depth to the bottom of the entire Iceland Basin (stations 29–38) and from 1800 to 3000 m depth within the Irminger Sea (stations 40–60). ISOW, despite having a fraction lower than 45 % above the Reykjanes Ridge (station 38), was the main contributor to the water mass pool from 1300 m depth down to the bottom. ISOW was also observed within the Labrador Sea from stations 68 to 77. Finally, the deepest part of the Irminger (stations 42 and 44) and Labrador (stations 68–71) seas was occupied by Denmark Strait Overflow Water (DSOW, $\theta \approx 1.30\,°C$, $S \approx 34.905$).

3.2 Ancillary data

3.2.1 Nitrate

Surface nitrate (NO_3^-) concentrations (García-Ibáñez et al., 2018; Pérez et al., 2018; Sarthou et al., 2018) ranged from 0.01 to $10.1\,\mu mol\,L^{-1}$ (stations 53 and 63, respectively). There was considerable spatial variability in NO_3^- surface distributions with high concentrations found in the Iceland Basin and Irminger Sea (higher than $6\,\mu mol\,L^{-1}$), as well as at stations 63 ($10.1\,\mu mol\,L^{-1}$) and 64 ($5.1\,\mu mol\,L^{-1}$), and low concentrations observed in the West European Basin, in the Labrador Sea, and above continental margins. The low surface concentrations in the West European Basin ranged from 0.02 (station 11) to 3.9 (station 25) $\mu mol\,L^{-1}$. Station 26 delineating the extreme western boundary of the West European Basin exhibited enhanced NO_3^- concentrations as a result of mixing between ENACW and IcSPMW, although these surface waters were dominated by ENACW. In the Labrador Sea (stations 68–78) low surface concentrations were observed with values ranging from 0.04 (station 68) to 1.8 (station 71) $\mu mol\,L^{-1}$. At depth, the lowest concentrations (lower than $15.9\,\mu mol\,L^{-1}$) were measured in ENACW ($\sim$ 0–800 m depth) and DSOW (> 1400 m depth), while the highest concentrations were measured within NEADW (up to $23.5\,\mu mol\,L^{-1}$) and in the mesopelagic zone of the West European and Iceland basins (higher than $18.4\,\mu mol\,L^{-1}$).

3.2.2 Chlorophyll *a*

Overall, most of the phytoplankton biomass was localized above 100 m depth with lower total chlorophyll *a* (TChl *a*) concentrations south of the Subarctic Front and higher at higher latitudes (see Supplement Fig. S1). While comparing TChl *a* maxima considering all stations, the lowest value ($0.35\,mg\,m^{-3}$) was measured within the West European Basin (station 19, 50 m depth) while the highest values were measured at the Greenland (up to $4.9\,mg\,m^{-3}$, 30 m depth, station 53, and up to $6.6\,mg\,m^{-3}$, 23 m depth, station 61) and Newfoundland (up to $9.6\,mg\,m^{-3}$, 30 m depth, station 78) margins.

3.3 Dissolved Fe concentrations

Dissolved Fe concentrations (see Supplement Table S1) ranged from $0.09 \pm 0.01\,nmol\,L^{-1}$ (station 19, 20 m depth) to $7.8 \pm 0.5\,nmol\,L^{-1}$ (station 78, 371 m depth) (see Fig. 3). Generally, vertical profiles of DFe for stations above the margins (2, 4, 53, 56, 61, and 78) showed an increase with depth, although sea-surface maxima were observed at stations 2, 4, and 56. For these margin stations, values ranged from 0.7 to $1.0\,nmol\,L^{-1}$ in the surface waters. Concentrations increased towards the bottom, with more than $7.8\,nmol\,L^{-1}$ measured at station 78; approximately 1–3 $nmol\,L^{-1}$ for stations 2, 4, 53, and 61; and just above $0.4\,nmol\,L^{-1}$ for station 56 (Fig. 4). Considering the four oceanic basins, mean vertical profiles (Fig. S2) showed increasing DFe concentrations down to 3000 m depth followed by decreasing DFe concentrations down to the bottom. Among deep-water masses, the lowest DFe concentrations were measured in the West European Basin. The Irminger Sea displayed the highest DFe concentrations from 1000 m depth to the bottom relative to other basins at similar depths (Figs. 3 and S2). In the Labrador Sea, DFe concentrations were low and relatively constant at about $0.87 \pm 0.06\,nmol\,L^{-1}$ from 250 to 3000 m depth (Fig. S2). Overall, surface DFe concentrations were higher ($0.36 \pm 0.18\,nmol\,L^{-1}$) in the North Atlantic Subpolar Gyre (above 52° N) than in the North Atlantic subtropical gyre ($0.17 \pm 0.05\,nmol\,L^{-1}$). The surface DFe concentrations were generally smaller than $0.3\,nmol\,L^{-1}$, except for a few stations in the Iceland Basin (stations 32 and 38) and Irminger (sta-

tions 40 and 42) and Labrador (station 63) seas, where values ranged between 0.4 and 0.5 nmol L^{-1}.

3.4 DFe signatures in water masses

In the Labrador Sea, IrSPMW exhibited an average DFe concentration of 0.61 ± 0.21 nmol L^{-1} ($n = 14$). DFe concentrations in the LSW were the lowest in this basin, with an average value of 0.71 ± 0.27 nmol L^{-1} ($n = 53$) (see Fig. S3). Deeper, ISOW displayed slightly higher average DFe concentrations (0.82 ± 0.05 nmol L^{-1}, $n = 2$). Finally, DSOW had the lowest average (0.68 ± 0.06 nmol L^{-1}, $n = 3$; see Fig. S3) and median (0.65 nmol L^{-1}) DFe values for intermediate and deep waters.

In the Irminger Sea, surface waters were composed of SAIW (0.56 ± 0.24 nmol L^{-1}, $n = 4$) and IrSPMW (0.72 ± 0.32 nmol L^{-1}, $n = 34$). The highest open-ocean DFe concentrations (up to 2.5 ± 0.3 nmol L^{-1}, station 44, 2600 m depth) were measured within this basin. In the upper intermediate waters, LSW was identified only at stations 40 to 44 and had the highest DFe values with an average of 1.2 ± 0.3 nmol L^{-1} ($n = 14$). ISOW showed higher DFe concentrations than in the Iceland Basin (1.3 ± 0.2 nmol L^{-1}, $n = 4$). At the bottom, DSOW was mainly located at stations 42 and 44 and presented the highest average DFe values (1.4 ± 0.4 nmol L^{-1}, $n = 5$) as well as the highest variability from all the water masses presented in this section (see Fig. S3).

In the Iceland Basin, SAIW and IcSPMW displayed similar averaged DFe concentrations (0.67 ± 0.30 nmol L^{-1}, $n = 7$ and 0.55 ± 0.34 nmol L^{-1}, $n = 22$, respectively). Averaged DFe concentrations were similar in both LSW and ISOW and higher than in SAIW and IcSPMW (0.96 ± 0.22 nmol L^{-1}, $n = 21$ and 1.0 ± 0.3 nmol L^{-1}, $n = 10$, respectively; see Fig. S3).

Finally, in the West European Basin, DFe concentrations in ENACW were the lowest of the whole section with an average value of 0.30 ± 0.16 nmol L^{-1} ($n = 64$). MOW was present deeper in the water column but was not characterized by particularly high or low DFe concentrations relative to the surrounding Atlantic waters (see Fig. S3). The median DFe value in MOW was very similar to the median value when considering all water masses (0.75 and 0.77 nmol L^{-1}, respectively, Fig. S3). LSW and IcSPMW displayed slightly elevated DFe concentrations compared to the overall median with mean values of 0.82 ± 0.08 ($n = 28$) and 0.80 ± 0.04 ($n = 8$) nmol L^{-1}, respectively. The DFe concentrations in NEADW were relatively similar to the DFe median value of the GEOVIDE voyage (0.71 and 0.77 nmol L^{-1}, respectively, Fig. S3).

4 Discussion

In the following sections, we will first discuss the high DFe concentrations observed throughout the water column of stations 1 and 17 located in the West European Basin (Sect. 4.1) and then the relationship between water masses and the DFe concentrations (Sect. 4.2) in intermediate (Sect. 4.2.2 and 4.2.3) and deep (Sect. 4.2.4 and 4.2.5) waters. We will also discuss the role of wind (Sect. 4.2.1), rivers (Sect. 4.3.1), meteoric water and sea ice processes (Sect. 4.3.2), atmospheric deposition (Sect. 4.3.3), and sediments (Sect. 4.4) in delivering DFe. Finally, we will discuss the potential Fe limitation using DFe : NO_3^- ratios (Sect. 4.5).

4.1 High DFe concentrations at stations 1 and 17

Considering the entire section, two stations (stations 1 and 17) showed irregularly high DFe concentrations (> 1 nmol L^{-1}) throughout the water column, thus suggesting analytical issues. However, these two stations were analyzed twice and provided similar results, therefore discarding any analytical issues. This means that these high values originated either from genuine processes or from contamination issues. If there had been contamination issues, one would expect a more random distribution of DFe concentrations and less consistence throughout the water column. It thus appears that contamination issues were unlikely to happen. Similarly, the influence of water masses to explain these distributions was discarded as the observed high homogenized DFe concentrations were restricted to these two stations. Station 1, located at the continental shelf break of the Iberian Margin, also showed enhanced PFe concentrations from lithogenic origin suggesting a margin source (Gourain et al., 2019). Conversely, no relationship was observed between DFe and PFe nor transmissometry for station 17. However, Ferron et al. (2016) reported a strong dissipation rate at the Azores-Biscay Rise (station 17) due to internal waves. The associated vertical energy fluxes could explain the homogenized profile of DFe at station 17, although such waves are not clearly evidenced in the velocity profiles. Consequently, the elevated DFe concentrations observed at station 17 remain unsolved.

4.2 DFe and hydrology key points

4.2.1 How do air–sea interactions affect DFe concentration in the Irminger Sea?

Among the four distinct basins described in this paper, the Irminger Sea exhibited the highest DFe concentrations within the surface waters (from 0 to 250 m depth) with values ranging from 0.23 to 1.3 nmol L^{-1} for open-ocean stations. Conversely, low DFe concentrations were previously reported in the central Irminger Sea by Rijkenberg et al. (2014) (April–May, 2010) and Achterberg et al. (2018) (April–May and July–August, 2010) with DFe concentrations ranging

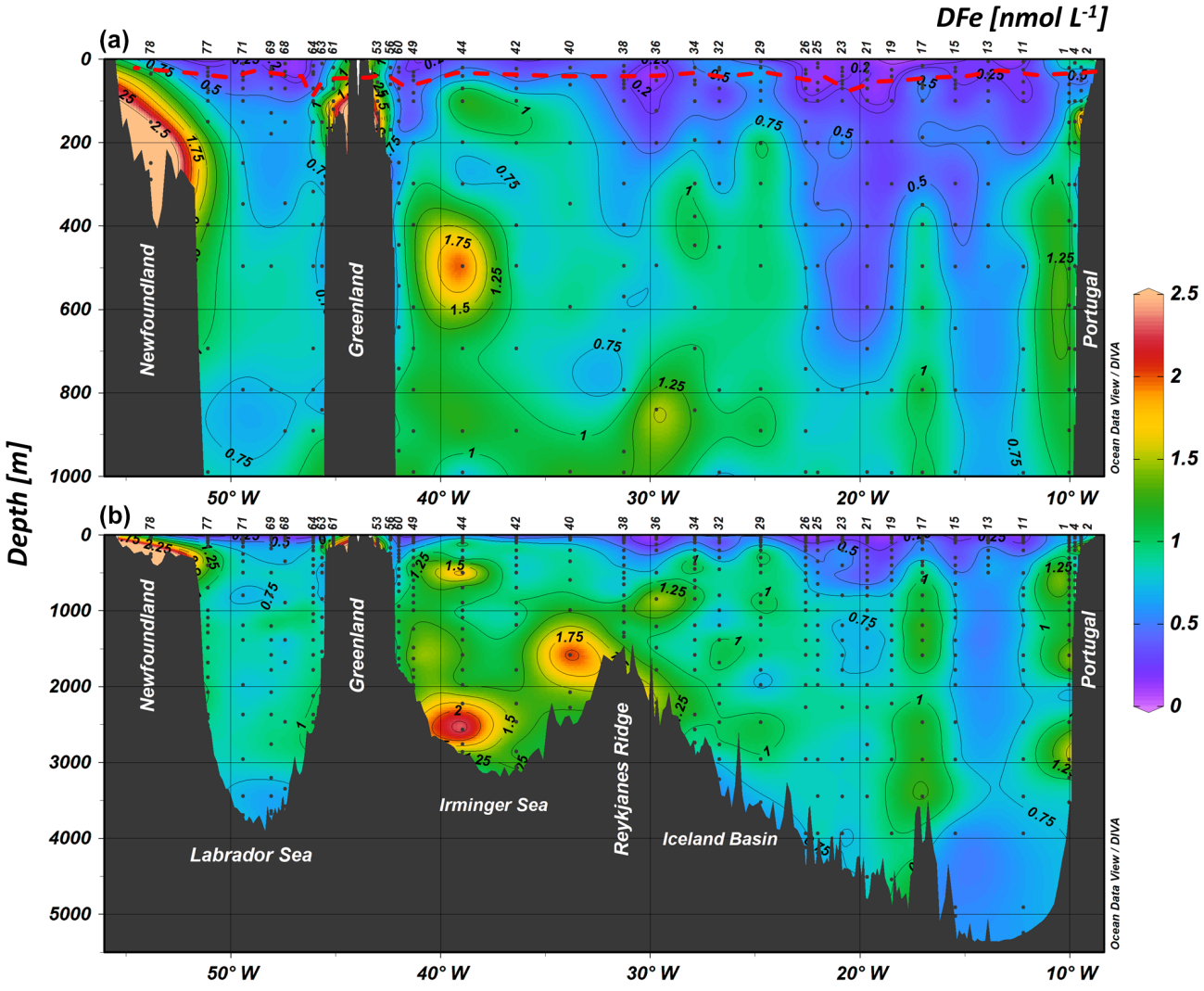

Figure 3. Contour plot of the distribution of dissolved iron (DFe) concentrations in nanomoles per liter along the GA01 voyage transect: upper 1000 m **(a)** and full depth range **(b)**. The red dashed line indicates the depth of the surface mixed layer (SML). Small black dots represent collected water samples at each sampling station (Ocean Data View (ODV) software, version 4.7.6; Schlitzer, 2016; http://odv.awi.de).

from 0.11 to 0.15 and from ∼ 0 to 0.14 nmol L^{-1}, respectively (see Fig. S4 and Table S2). Differences might be due to the phytoplankton bloom advancement, the high remineralization rate (Lemaitre et al., 2018b) observed within the LSW in the Irminger Sea (see Sect. 4.1.3), and a deeper winter convection in early 2014. Indeed, enhanced surface DFe concentrations measured during GEOVIDE in the Irminger Sea could be due to intense wind forcing events that would deepen the winter Z_m down to the core of the Fe-rich LSW.

In the North Atlantic Ocean, the warm and salty water masses of the upper limb of the AMOC are progressively cooled and become denser, and they subduct into the abyssal ocean. In some areas of the subpolar North Atlantic, deep convective winter mixing provides a rare connection between surface and deep waters of the AMOC, thus constituting an important mechanism in supplying nutrients to the surface ocean (de Jong et al., 2012; Louanchi and Najjar, 2001). Deep convective winter mixing is triggered by the effect of wind and a preconditioning of the ocean in such a way that the inherent stability of the ocean is minimal. Pickart et al. (2003) demonstrated that these conditions are satisfied in the Irminger Sea with the presence of weakly stratified surface water, a close cyclonic circulation, which leads to the shoaling of the thermocline, and intense winter air–sea buoyancy fluxes (Marshall and Schott, 1999). Moore (2003) and Piron et al. (2016) described low-altitude westerly jets centered northeast of Cape Farewell, over the Irminger Sea, known as tip jet events. These events occur when wind is split around the orographic features of Cape Farewell and are strong enough to induce deep convective mixing (Bacon et al., 2003; Pickart et al., 2003). It has also been shown that during winters with a positive North Atlantic Oscilla-

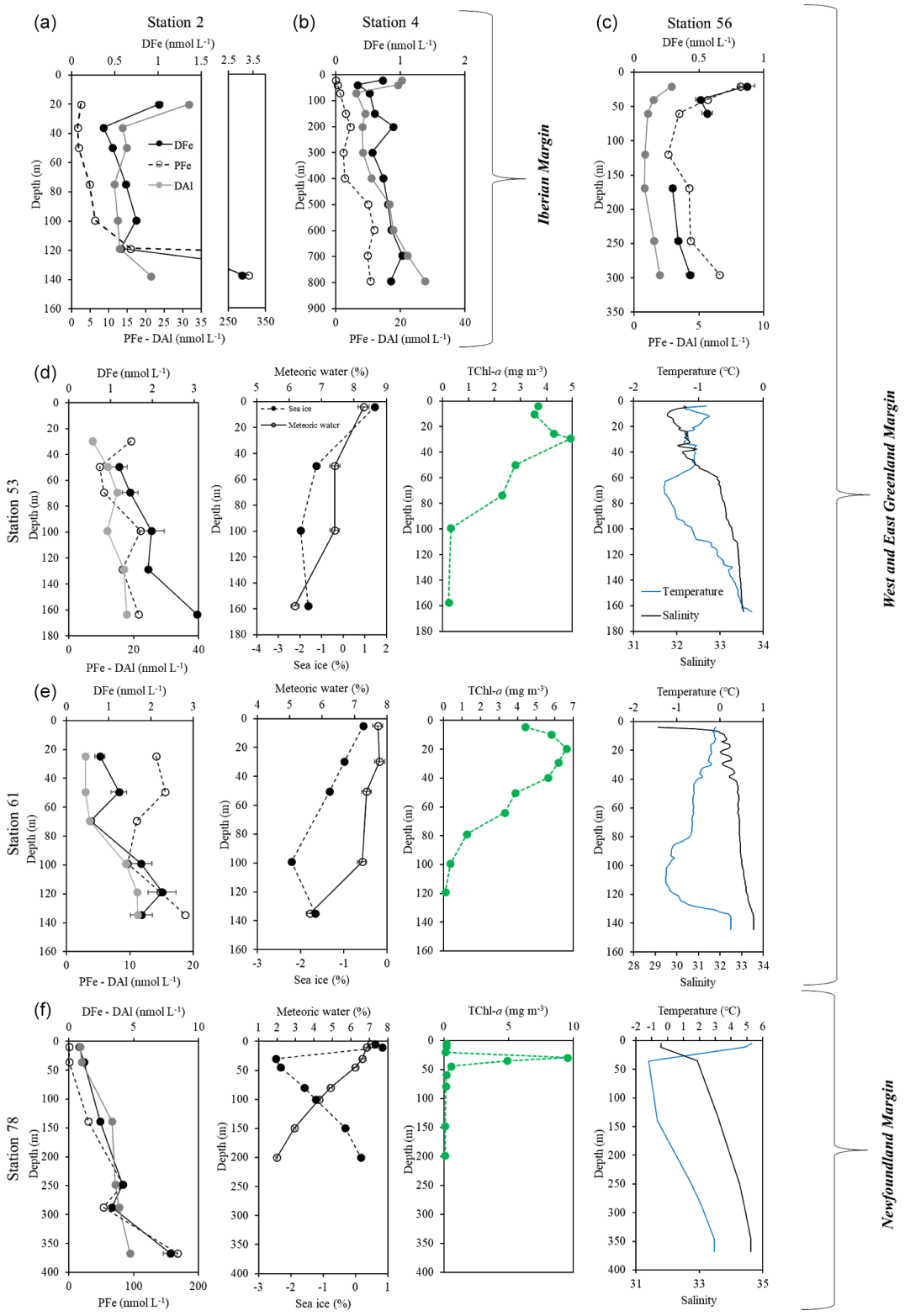

Figure 4. Vertical profiles of dissolved iron (DFe, black dots, solid line), particulate iron (PFe, black open dots, dashed line; Gourain et al., 2019), and dissolved aluminum (DAl, grey dots; Menzel Barraqueta et al., 2018) at stations 2 **(a)**, and 4 **(b)** located above the Iberian shelf; station 56 **(c)**, station **(d)** 53 and station 61 **(e)** located above the Greenland shelf; and station 78 **(f)** located above the Newfoundland shelf. Note that for stations 53, 61, and 78, plots of the percentage of meteoric water (open dots) and sea ice melting (black dots and dashed line) (Benetti et al., 2017, see text for details), total chlorophyll *a* (TChl *a*, green), temperature (blue), and salinity (black) are also displayed as a function of depth.

tion (NAO) index, the occurrence of such events is favored (Moore, 2003; Pickart et al., 2003), which was the case in the winter of 2013–2014, preceding the GEOVIDE voyage as opposed to previous studies (Pascale Lherminier, personal communication, 2019). The winter mixed-layer depth prior to the cruise reached up to 1200 m depth in the Irminger Sea (Zunino et al., 2017), which was most likely attributed to a final deepening due to wind forcing events (centered at station 44). Such winter entrainment was likely the process involved in the vertical supply of DFe within surface waters fueling the spring phytoplankton bloom with DFe values close to those found in LSW.

4.2.2 Why do we not see a DFe signature in the Mediterranean Overflow Water (MOW)?

On its northern shores, the Mediterranean Sea is bordered by industrialized European countries, which act as a continuous source of anthropogenically derived constituents into the atmosphere, and on the southern shores by the arid and desert regions of the north African and Arabian Desert belts, which act as sources of crustal material in the form of dust pulses (Chester et al., 1993; Guerzoni et al., 1999; Martin et al., 1989). During the summer, when thermal stratification occurs, DFe concentrations in the SML can increase over the whole Mediterranean Sea by 1.6–5.3 nmol L^{-1} in response to the accumulation of atmospheric Fe from both anthropogenic and natural origins (Bonnet and Guieu, 2004; Guieu et al., 2010; Sarthou and Jeandel, 2001). After atmospheric deposition, the fate of Fe will depend on the nature of aerosols, Fe–ligand binding capacity, vertical mixing, biological uptake, and scavenging processes (Bonnet and Guieu, 2006; Wuttig et al., 2013). During GEOVIDE, MOW was observed at percentages higher than $\sim 60\,\%$ from stations 1 to 13 between 900 and 1100 m depth and associated with high dissolved aluminum (DAl; Menzel Barraqueta et al., 2018) concentrations (up to 38.7 nmol L^{-1}), confirming the high atmospheric deposition in the Mediterranean region. In contrast to Al, no DFe signature was associated with MOW (Figs. 2 and 3). Using LADCP data during the cruise, we estimated a translation velocity for the MOW of $\sim$ 3–8 cm s^{-1}, consistent with previous published values (e.g., Armi et al., 1989; Schmidt et al., 1996). Our station 13 was located $\sim$ 2000 km away from the origin of the MOW, which would mean a transit time of $\sim$ 1–2 years. This transit time would allow the Fe signal to be preserved, when DFe residence times range from weeks to months in the surface waters and from tens to hundreds of years in deep waters (de Baar and de Jong, 2001; Sarthou et al., 2003; Croot et al., 2004; Bergquist and Boyle 2006; Gerringa et al., 2015; Tagliabue et al., 2016). This feature was also reported in some studies (Hatta et al., 2015; Thuróczy et al., 2010), while others measured higher DFe concentrations in MOW (Gerringa et al., 2017; Sarthou et al., 2007). However, MOW coincides with the maximum apparent oxygen utilization (AOU) and it is not possible to distinguish the MOW signal from the remineralization signal (Sarthou et al., 2007). On the other hand, differences between studies likely originate from the intensity of atmospheric deposition and the nature of aerosols. Indeed, Wagener et al. (2010) highlighted that large dust deposition events can accelerate the export of Fe from the water column through scavenging. As a result, in seawater with high DFe concentrations and where high dust deposition occurs, a strong individual dust deposition event could act as a sink for DFe. It thus becomes less evident to observe a systematic high-DFe signature in MOW despite dust inputs.

4.2.3 Fe enrichment in Labrador Sea Water (LSW)

As described in Sect. 3.1, the LSW exhibited increasing DFe concentrations from its source area, the Labrador Sea, toward the other basins, with the highest DFe concentrations observed within the Irminger Sea, suggesting that the water mass was enriched in DFe either locally in each basin or during its flow path (see Fig. S3). These DFe sources could originate from a combination of high export of PFe and its remineralization in the mesopelagic area and/or the dissolution of sediment.

The Irminger and Labrador seas exhibited the highest averaged integrated TChl-a concentrations (98 ± 32 and 59 ± 42 mg m^{-2}) compared to the West European and Iceland basins (39 ± 10 and 53 ± 16 mg m^{-2}), when the influence of margins was discarded. Stations located in the Irminger (stations 40–56) and Labrador (stations 63–77) seas were largely dominated by diatoms (> 50 % of phytoplankton abundances) and displayed the highest chlorophyllide *a* concentrations, a tracer of senescent diatom cells, likely reflecting post-bloom conditions (Tonnard et al., in prep.). This is in line with the highest POC export data reported by Lemaitre et al. (2018a) in these two oceanic basins. This likely suggests that biogenic PFe export was also higher in the Labrador and Irminger seas than in the West European and Iceland basins. In addition, Gourain et al. (2019) highlighted a higher biogenic contribution for particles located in the Irminger and Labrador seas with relatively high PFe : PAl ratios (0.44 ± 0.12 mol : mol and 0.38 ± 0.10 mol : mol, respectively) compared to particles from the West European and Iceland basins (0.22 ± 0.10 and 0.38 ± 0.14 mol : mol, respectively; see Fig. 6a in Gourain et al., 2019). However, they reported no difference in PFe concentrations between the four oceanic basins, when the influence of margins was discarded, which likely highlighted the remineralization of PFe within the Irminger and Labrador seas. Indeed, Lemaitre et al. (2018b) reported higher remineralization rates within the Labrador (up to 13 mmol C m^{-2} d^{-1}) and Irminger seas (up to 10 mmol C m^{-2} d^{-1}) using the excess barium proxy (Dehairs et al., 1997), compared to the West European and Iceland basins (ranging from 4 to 6 mmol C m^{-2} d^{-1}). Therefore, the intense remineralization rates measured in the

Irminger and Labrador seas likely resulted in enhanced DFe concentrations within LSW.

Higher DFe concentrations were, however, measured in the Irminger Sea compared to the Labrador Sea and coincided with lower transmissometry values (i.e., 98.0 %–98.5 % vs. > 99 %), thus suggesting a particle load of the LSW. This could be explained by the reductive dissolution of Newfoundland Margin sediments. Indeed, Lambelet et al. (2016) reported high dissolved neodymium (Nd) concentrations (up to 18.5 pmol kg^{-1}) within the LSW at the edge of the Newfoundland Margin (51.82° N, 45.73° W) as well as slightly lower Nd isotopic ratio values relative to those observed in the Irminger Sea. They suggested that this water mass had been in contact with sediments approximately within the last 30 years (Charette et al., 2015). Similarly, during GA03, Hatta et al. (2015) attributed the high DFe concentrations in the LSW to continental margin sediments. Consequently, it is also possible that the elevated DFe concentrations from the three LSW branches which entered the West European and Iceland basins and Irminger Sea were supplied through sediment dissolution (Measures et al., 2013) along the LSW pathway.

The enhanced DFe concentrations measured in the Irminger Sea and within the LSW were thus likely attributed to the combination of higher productivity, POC export, and remineralization as well as a DFe supply from reductive dissolution of Newfoundland sediments to the LSW along its flow path. Using temperature and salinity anomalies, Yashayaev et al. (2007) showed that the LSW reached the Irminger Sea and the Iceland Basin in 1–2 and 4–5 years, respectively, after its formation in the Labrador Sea. The LSW transit time in this region is thus compatible with DFe residence times (see above).

4.2.4 Enhanced DFe concentrations in the Irminger Sea bottom water

Bottom waters from the Irminger Sea exhibited the highest DFe concentrations from the whole section, excluding the stations at the margins. Such a feature could be due to (i) vertical diffusion from local sediment, (ii) lateral advection of water mass(es) displaying enhanced DFe concentrations, and (iii) local dissolution of Fe from particles. Hereafter, we discuss the plausibility of these three hypotheses.

The GEOTRACES GA02 voyage (leg 1, 64PE319) which occurred in April–May 2010 from Iceland to Bermuda sampled two stations north and south of our station 44 (59.62° N, ∼ 38.95° W): station 5 (60.43° N, ∼ 37.91° W) and 6 (58.60° N, ∼ 39.71° W), respectively. High DFe concentrations in samples collected close to the bottom were also observed and attributed to sediment inputs highlighting boundary exchange between seawater and surface sediment (Lambelet et al., 2016; Rijkenberg et al., 2014). However, because a decrease in DFe concentrations was observed at our station 44 from 2500 m depth down to the bottom (Fig. 3 and Table S1), it appeared to be unlikely that these high DFe concentrations are the result of local sediment inputs, as no DFe gradient from the deepest samples to those above was observed.

Looking at salinity versus depth for these three stations, one can observe the intrusion of Polar Intermediate Water (PIW) at station 44 during GEOVIDE, which was not observed during the GA02 voyage and which contributed to about 14 % of the water mass composition (García-Ibáñez et al., 2018) and might therefore be responsible for the high DFe concentrations (see Fig. S5a). On the other hand, the PIW was also observed at stations 49 (from 390 to 1240 m depth), 60 (from 440 to 1290 m depth), 63 (from 20 to 1540 m depth), 68 (3340 m depth), 69 (from 3200 to 3440 m depth), 71 (from 2950 to 3440 m depth), and 77 (60 and 2500 m depth) with similar or higher contributions of the PIW without such high DFe concentrations (maximum DFe $= 1.3 \pm 0.1$ nmol L^{-1}, 1240 m depth at station 49). At this station, the DSOW relative abundance was more than 20 % (Fig. S5). The overflow of this dense water in the Irminger Sea is associated with intense cyclonic boluses (Käse et al., 2003) and the entrainment of waters from the Greenland margin and slope by pulses of DSOW occurs all along its transport from Denmark Strait to the Greenland tip (Magaldi et al., 2011; von Appen et al., 2014). This phenomenon may enrich the DSOW with Fe as well as other elements. This was also observed for radium and actinium with a deviation from the conservative behavior of ^{226}Ra (Le Roy et al., 2018) and an increase in ^{227}Ac activity at station 44 at 2500 m, reflecting inputs of these tracers. Therefore, the high DFe concentrations observed in the Irminger Sea might be inferred from a substantial load of Fe-rich particles when DSOW is in contact with the Greenland margin.

4.2.5 Reykjanes Ridge: hydrothermal inputs or Fe-rich seawater?

Hydrothermal activity was assessed over the Mid-Atlantic Ridge, namely the Reykjanes Ridge (RR), from stations 36 to 40. Indeed, within the inter-ridge database (http://www.interridge.org, last access: 30 January 2020), the Reykjanes Ridge is reported to have active hydrothermal sites. The sites were either confirmed (Baker and German, 2004; German et al., 1994; Olaffson et al., 1991; Palmer et al., 1995) close to Iceland or inferred (e.g., Chen, 2003; Crane et al., 1997; German et al., 1994; Sinha et al., 1997; Smallwood and White, 1998) closer to the GEOVIDE section as no plume was detected but a high backscatter was reported, potentially corresponding to a lava flow. Therefore, hydrothermal activity at the sampling sites remains unclear with no elevated DFe concentrations nor temperature anomaly above the ridge (station 38). However, enhanced DFe concentrations (up to 1.5 ± 0.22 nmol L^{-1}, station 36, 2200 m depth) were measured east of the Reykjanes Ridge (Fig. 3). This could be due to hydrothermal activity and resuspension of sunken par-

ticles at sites located north of the section and transported through ISOW towards the section (Fig. 3). Indeed, Achterberg et al. (2018) highlighted at ∼ 60° N and over the Reykjanes Ridge a southward lateral transport of a Fe plume of up to 250–300 km. In agreement with these observations, previous studies (e.g., Fagel et al., 1996, 2001; Lackschewitz et al., 1996; Parra et al., 1985) reported marine sediment mineral clays in the Iceland Basin largely dominated by smectite (> 60 %), a tracer of hydrothermal alteration of basaltic volcanic materials (Fagel et al., 2001; Tréguer and De La Rocha, 2013). Kanzow and Zenk (2014) investigated the fluctuations of the ISOW plume around RR. The transit time, west of RR, between 60° N and the Bight Fracture Zone (BFZ), was around 5 months, compatible with the residence time of DFe (see above). Hence, the high DFe concentrations measured east of RR could be due to a hydrothermal source and/or the resuspension of (basaltic) particles and their subsequent dissolution.

West of the Reykjanes Ridge, a DFe enrichment was also observed in ISOW at station 40 within the Irminger Sea (Fig. 3). The low transmissometer values within ISOW in the Irminger Sea (station 44) compared to the Iceland Basin (station 32) suggested a higher particle load (Fig. 4a in Gourain et al., 2019). These particles could come from the Bight Fracture Zone (BFZ, 56.91° N and 32.74° W) (Fig. 1) (Lackschewitz et al., 1996; Zou et al., 2017) since the transit time of the ISOW between BFZ and our station 40 is around 3 months (Kanzow and Zenk, 2014).

4.3 What are the main sources of DFe in surface waters?

During GEOVIDE, enhanced DFe surface concentrations were observed at several stations (stations 1–4, 53, 61, 78) highlighting an external source of Fe to surface waters. The main sources able to deliver DFe to surface waters are riverine inputs, glacial inputs, and atmospheric deposition. In the following sections, these potential sources of DFe to surface waters will be discussed.

4.3.1 Tagus riverine inputs

Enhanced DFe surface concentrations (up to 1.07 ± 0.12 nmol L^{-1}) were measured over the Iberian Margin (stations 1–4) and coincided with salinity minima (∼ <35) and enhanced DAl concentrations (up to 31.8 nmol L^{-1}; Menzel Barraqueta et al., 2018). DFe and DAl concentrations were both significantly negatively correlated with salinity ($R^2 =$∼ 1 and 0.94, respectively) from stations 1 to 13 (Fig. 5). Salinity profiles from stations 1 to 4 showed evidence of a freshwater source with surface salinity ranging from 34.95 (station 1) to 35.03 (station 4). Within this area, only two freshwater sources were possible: (1) wet atmospheric deposition (four rain events; Rachel Shelley, personal communication, 2019) and (2) the Tagus River, since the shipboard acoustic Doppler current profiler (SADCP) data revealed a northward circulation with a velocity of around 0.1 m s^{-1} (Pascale Lherminier, Patricia Zunino, personal communication, 2019). The transit time from the estuary to our stations above the shelf is around 15 d (150 km), which is short enough to preserve the DFe signal. Our SML DFe inventories were about 3 times higher at station 1 (∼ 1 nmol L^{-1}) than those calculated during the GA03 voyage (∼ 0.3 nmol L^{-1}, station 1). Atmospheric deposition was about 1 order of magnitude higher during GA03 than during GA01 (Shelley et al., 2015, 2018); thus the atmospheric source seemed to be minor during GA01. Consequently, the Tagus River appears as the most likely source responsible for these enhanced DFe concentrations, either directly as input of DFe or indirectly through Fe-rich sediment carried by the Tagus River and its subsequent dissolution. The Tagus estuary is the largest in the western European coast and very industrialized (Canário et al., 2003; de Barros, 1986; Figueres et al., 1985; Gaudencio et al., 1991; Mil-Homens et al., 2009); it extends through an area of 320 km^2 and is characterized by a large water flow of 15.5×10^9 m^3 yr^{-1} (Fiuza, 1984). Many types of industry (e.g., heavy metallurgy, ore processing, chemical industry) release metals including Fe, which therefore result in high levels recorded in surface sediments, suspended particulate matter, water, and organisms in the lower estuary (Santos-Echeandia et al., 2010).

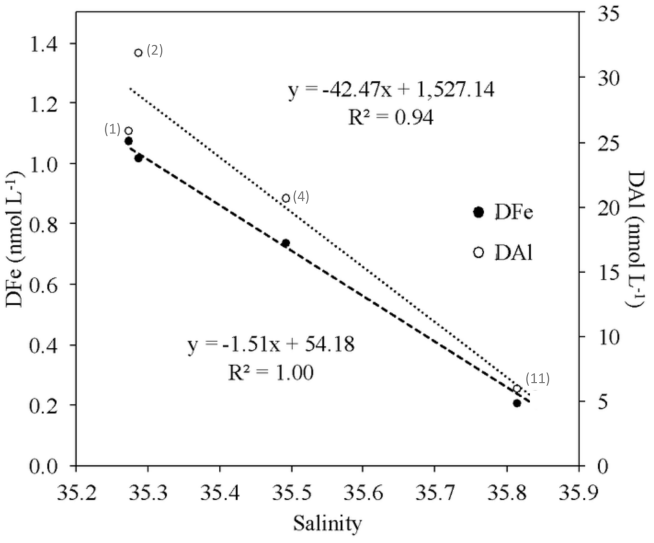

Figure 5. Plot of dissolved iron (DFe, filled circles) and dissolved aluminum (DAl, open circles; Menzel Barraqueta et al., 2018) at ∼ 20 m, along the salinity gradient between stations 1, 2, 4, and 11 with linear regression equations. The numbers close to sample points represent the station numbers.

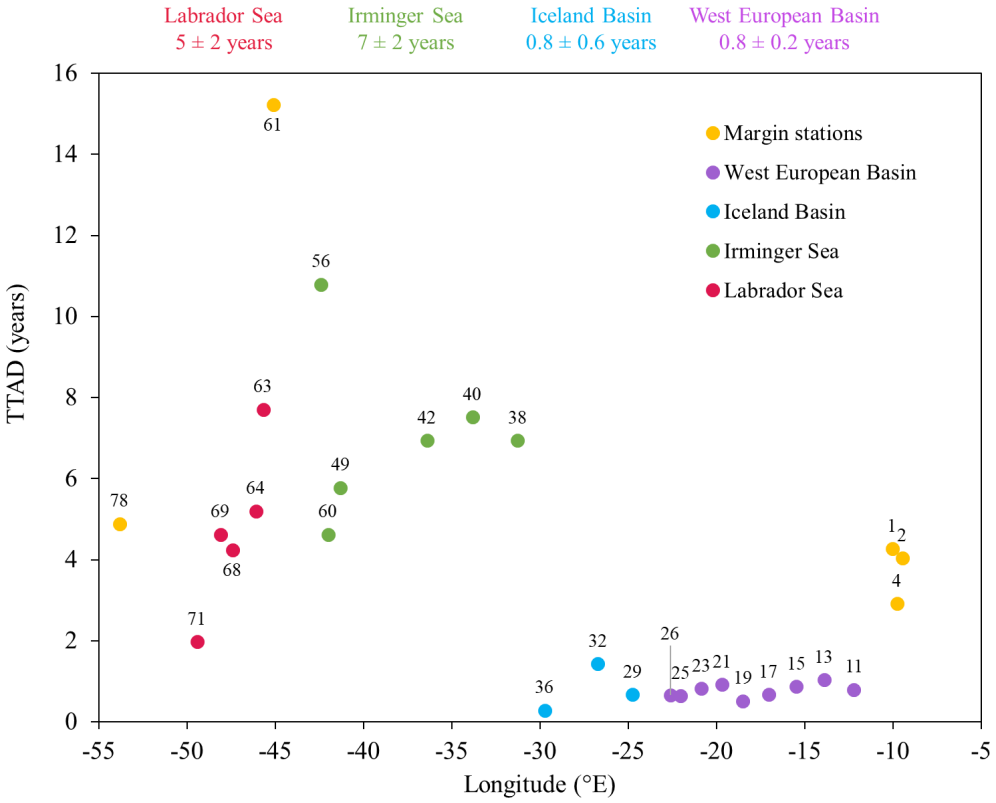

Figure 6. Plot of dissolved Fe (DFe) turnover times relative to atmospheric deposition (TTADs) calculated from soluble Fe contained in aerosols estimated from a two-stage sequential leach (UHPW, then 25 % HAc; Shelley et al., 2018). Note that numbers on top of points represent station numbers and that the color coding refers to different regions with margin stations in yellow, the West European Basin in purple, the Iceland Basin in blue, the Irminger Sea in green, and the Labrador Sea in red. The numbers on top of the plot represent TTADs averaged for each oceanic basin and their standard deviation.

4.3.2 High-latitude meteoric water and sea ice processes

Potential sources of Fe at stations 53, 61, and 78 include meteoric water (MW, referring to precipitation, runoff, and continental glacial melt), sea ice melt (SIM), seawater interaction with shallow sediments, and advection of water transported from the Arctic sourced by the Fe-rich Transpolar Drift (TPD; Klunder et al., 2012; see Fig. S4 and Table S2). The vertical profiles of both potential temperature and salinity in the Greenland and Newfoundland margins (stations 53, 61, and 78; Fig. 4d, e, and f) highlighted the presence of this freshwater lens likely originating from the Arctic Ocean. They were present in the upper 60 m (station 53) and 40 m (stations 61 and 78) depth. The most plausible source of this freshwater lens would be meteoric water and sea ice melting. Deeper in the water column, net brine release (defined as a negative value of sea ice melting) was observed at stations 53 (below 40 m depth, Fig. 4d), 61 (in the whole water column, Fig. 4e), and 78 (below 30 m depth, Fig. 4f). The release of brines could originate from two different processes: the sea ice formation or the early melting of multiyear sea ice due to gravitational drainage and subsequent brine release (Petrich and Eicken, 2010; Wadhams, 2000). Indeed, during the winter preceding the GEOVIDE voyage, multiyear sea ice extended 200 km off the Greenland stations (http://nsidc.org/arcticseaicenews/, last access: 30 Janauary 2020). In the following sections, we discuss the potential for meteoric water supply, sea ice formation, and sea ice melting to affect DFe distribution.

The Greenland shelf

Considering the sampling period at stations 53 (16 June 2014) and 61 (19 June 2014), sea ice formation is unlikely to happen as this period coincides with summer melting in both the central Arctic and East Greenland (Markus et al., 2009). However, it is possible that the brines observed in our study could originate from sea ice formation which occurred during the previous winter(s) at 66° N (and/or higher latitudes). The brine signal at station 61 between 40 and 140 m was associated with a depletion in both DFe and PFe, which may be attributed to sea ice formation processes. Indeed, as soon as sea ice forms, sea salts are efficiently flushed out of the ice while PFe is trapped

within the crystal matrix and DFe accumulates, leading to an enrichment factor of these two Fe fractions compared to underlying seawater (Janssens et al., 2016). Conversely, the strongest brine signal observed at station 53 (between 50 and 160 m) showed slight enrichments in both DFe and PFe, which may be attributed to sea ice melting and the associated release into the underlying water column.

Surface waters at stations 53 and 61 were characterized by high MW fractions together with enrichments in PFe at station 53 and in both DFe and PFe at station 61 (Fig. 4d and e). These results are in line with previous observations, which highlighted strong inputs of DFe from a meteoric water melting source in Antarctica (Annett et al., 2015). At station 61, the relative depletion of DFe at 30 m compared to 50 m may be due to phytoplankton uptake, as indicated by the high TChl *a* concentrations (up to 6.6 mg m^{-3}, Fig. 4d). Hence, it seemed that meteoric water inputs from the Greenland Margin likely fertilized surface waters with DFe, enabling the phytoplankton bloom to subsist.

The Newfoundland shelf

Newfoundland shelf waters (station 78) were characterized by high MW fractions (up to 7 %), decreasing from surface to 200 m depth (~ 2 %). These waters were associated with a net sea ice melting signal from the near surface to ~ 10 m depth followed by a brine release signal down to 200 m depth with the maximum contribution measured at ~ 30 m depth. Within the surface waters (above 20 m depth), no elevation in DFe, DAl, nor PFe was noticed despite the low measured TChl *a* concentrations (TChl $a \sim 0.20$ mg m^{-3}). This suggests that none of these inputs (sea ice melting and meteoric water) were able to deliver DFe or that these inputs were minor compared to sediment inputs from the Newfoundland Margin. Surprisingly, the highest TChl *a* biomass (TChl $a > 9$ mg m^{-3}) from the whole section was measured at 30 m depth corresponding to the strongest brine release signal. This suggests either that the brine likely contained important amounts of Fe (dissolved and/or particulate Fe) that were readily available for phytoplankton and consumed at the sampling period by potentially sea ice algae themselves (Riebesell et al., 1991) or that another nutrient was triggering the phytoplankton bloom.

4.4 Atmospheric deposition

On a regional scale, the North Atlantic basin receives the largest amount of atmospheric inputs due to its proximity to the Sahara (Jickells et al., 2005), yet even in this region of high atmospheric deposition, inputs are not evenly distributed. Indeed, aerosol Fe loading measured during GEOVIDE (Shelley et al., 2017) was much lower (up to 4 orders of magnitude) than that measured during studies from lower latitudes in the North Atlantic (e.g., Baker et al., 2013; Buck et al., 2010; and for GA03, Shelley et al., 2015), but atmospheric inputs could still be an important source of Fe to surface waters in areas far from land.

In an attempt to estimate whether there was enough atmospheric input to sustain the SML DFe concentrations, we calculated turnover times relative to atmospheric deposition (TTADs; Guieu et al., 2014). To do so, we made the following assumptions: (1) the aerosol concentrations are a snapshot in time but are representative of the study region, (2) the aerosol solubility estimates based on two sequential leaches are an upper limit of the aerosol Fe in seawater, and (3) the water column stratified just before the deposition of atmospheric inputs, so DFe in the mixed layer will reflect inputs from above. Thus, the TTADs were defined as the integrated DFe concentrations in the SML for each station divided by the contribution of soluble Fe contained in aerosols averaged per basin to the water volume of the SML. Although TTADs were lower in the West European and Iceland basins with an average of $\sim 9 \pm 3$ months compared to other basins (7 ± 2 and 5 ± 2 years for the Irminger and Labrador seas, respectively) (Fig. 6), they were about 3 times higher than those reported for areas impacted by Saharan dust inputs (~ 3 months; Guieu et al., 2014). Therefore, the high TTADs measured in the Irminger and Labrador seas and ranging from 2 to 15 years provided further evidence that atmospheric deposition was unlikely to supply Fe in a sufficient quantity to be the main source of DFe (see Sect. 4.2.1 and 4.3.2), while in the West European and Iceland basins they were an additional source, perhaps the main source of Fe, especially at station 36 which displayed TTAD of 3 months.

4.4.1 Sediment input

Margins

DFe concentration profiles from all coastal stations (stations 2, 4, 53, 56, 61, and 78) are reported in Fig. 4. To avoid surface processes, only depths below 100 m depth will be considered in the following discussion. DFe and PFe followed a similar pattern at stations 2, 53, 56, and 78 with increasing concentrations towards the sediment, suggesting that either the sources of Fe supplied both Fe fractions (dissolved and particulate) or that PFe dissolution from sediments supplied DFe. Among the different margins, the Newfoundland Margin exhibited the highest deep-water DFe and PFe concentrations. Conversely, stations 4 and 61 exhibited a decrease in DFe concentrations in the samples closest to the seafloor whereas PFe increased. DFe : PFe ratios ranged from 0.01 (station 2, bottom sample) to 0.27 (station 4, ~ 400 m depth) mol : mol with an average value of 0.11 ± 0.07 mol : mol ($n = 23$, Table 3). This could be explained by the different nature of the sediments and/or different sediment conditions (e.g., redox, organic content). Based on particulate and dissolved Fe and dissolved Al data (Gourain et al., 2019; Menzel Barraqueta et al., 2018, Table 3), three main different types of margins were reported (Gourain et

al., 2019) with the highest lithogenic contribution observed at the Iberian Margin (stations 2 and 4) and the highest biogenic contribution at the Newfoundland Margin (station 78). These observations are consistent with higher TChl *a* concentrations measured at the Newfoundland Margin and to a lesser extent at the Greenland Margin and the predominance of diatoms relative to other functional phytoplankton classes at both margins (Tonnard et al., 2020). To sum up, the more biogenic sediments (Newfoundland Margin) were able to mobilize more Fe in the dissolved phase than the more lithogenic sediments (Iberian Margin), in agreement with Boyd et al. (2010), who reported greater remineralization of PFe from biogenic PFe than from lithogenic PFe based on field experiment and modeling simulations.

4.4.2 Nepheloid layers

Samples associated with high levels of particles (transmissometer < 99 %) and below 500 m depth displayed a huge variability in DFe concentrations. From the entire dataset, 63 samples ($\sim$ 13 % of the entire dataset) followed this criterion with 14 samples from the West European Basin (station 1), four samples from the Iceland Basin (stations 29, 32, 36, and 38), 43 samples from the Irminger Sea (stations 40, 42, 44, 49, and 60), and two samples from the Labrador Sea (station 69). To determine which parameter was susceptible to explain the variation in DFe concentrations in these nepheloid layers, a principal component analysis (PCA) was performed on these samples. The input variables of the PCA were particulate Fe, Al, and manganese (PMn) (Gourain et al., 2019); DAl (Menzel Barraqueta et al., 2018); and apparent oxygen utilization (AOU) and were all correlated to DFe concentrations explaining all together 93 % of the subset variance (see Fig. S6). The first dimension of the PCA was represented by PAl, PFe, and PMn concentrations and explained 59.5 % of the variance, while the second dimension was represented by the DAl and the AOU parameters, explaining 33.2 % of the variance. The two sets of variables were nearly at a right angle from each other, indicating no correlation between them.

The variations in DFe concentrations measured in bottom samples from stations 32, 36 (Iceland Basin), 42, 44 (Irminger Sea), and 69 (Labrador Sea) were mainly explained by the first dimension of the PCA (see Fig. S6). Therefore, samples characterized by the lowest DFe concentrations (stations 32 and 69) were driven by particulate Al and Mn concentrations and resulted in an enrichment of Fe in the particulate phase. These results are in agreement with previous studies showing that the presence of Mn within particles can induce the formation of Fe–Mn oxides, contributing to the removal of Fe and Mn from the dissolved phase (Kan et al., 2012; Teng et al., 2001).

Low DFe concentrations (bottom samples from stations 42 and 1) were linked to DAl inputs and associated with lower AOU values. The release of Al has previously been observed from Fe and Mn oxide coatings on resuspended sediments under mildly decreasing conditions (Van Beusekom, 1988). Conversely, higher DFe concentrations were observed for stations 44 and 49 and to a lesser extent station 60 coinciding with low DAl inputs and higher oxygen levels. This observation challenges the traditional view of Fe oxidation with oxygen, either abiotically or microbially induced. Indeed, remineralization can decrease sediment oxygen concentrations, promoting reductive dissolution of PFe oxyhydroxides to DFe that can then diffuse across the sediment–water interface as DFe(II) colloids (Homoky et al., 2011). Such processes will inevitably lead to rapid Fe removal through precipitation of nanoparticulate or colloidal Fe (oxyhydr)oxides, followed by aggregation or scavenging by larger particles (Boyd and Ellwood, 2010; Lohan and Bruland, 2008) unless complexion with Fe-binding organic ligands occurs (Batchelli et al., 2010; Gerringa et al., 2008). There is, however, another process that is favored in oxic benthic boundary layers (BBLs) with low organic matter degradation and/or low Fe oxides, which implies the dissolution of particles after resuspension, namely the non-reductive dissolution of sediment (Homoky et al., 2013; Radic et al., 2011). In addition, these higher oxygenated samples were located within DSOW, which mainly originates (75 % of the overflow) from the Nordic Seas and the Arctic Ocean (Tanhua et al., 2005), in which the ultimate source of Fe was reported by Klunder et al. (2012) to come from Eurasian river waters. The major Arctic rivers were highlighted by Slagter et al. (2017) to be a source of Fe-binding organic ligands that are then further transported via the TPD across the Denmark Strait. Hence, the enhanced DFe concentrations measured within DSOW might result from Fe-binding organic ligand complexation that was transported to the deep ocean as DSOW formed rather than the non-reductive dissolution of sediment.

4.5 How does biological activity modify DFe distribution?

Overall, almost all the stations from the GEOVIDE voyage displayed DFe minima in surface water associated with some maxima of TChl *a* (see Fig. S1). In the following section, we specifically address the question of whether DFe concentrations potentially limit phytoplankton growth. Note that macronutrients and DFe limitations relative to phytoplankton functional classes are dealt with (Tonnard et al., 2020).

A key determinant for assessing the significance of a DFe source is the magnitude of the DFe : macronutrient ratio supplied, since this term determines to which extent DFe will be utilized. The DFe : NO_3^- ratios in surface waters varied from 0.02 (station 36) to 38.6 (station 61) mmol : mol with an average of 5 ± 10 mmol : mol (see Fig. S7). Values were typically equal to or lower than 0.28 mmol mol^{-1} in all basins except at the margins and at stations 11, 13, 68, 69, and 77. The low nitrate concentrations observed at the eastern and western Greenland and Newfoundland margins reflected a strong phytoplankton bloom which had reduced the con-

Table 3. Averaged DFe : DAl (Menzel Barraqueta et al., 2018) and PFe : PAl (Gourain et al., 2020) ratios reported per margin. Note that to avoid phytoplankton uptake, only depths below 100 m depth are considered.

Margins	Station no.	DFe : DAl (mol : mol) average SD	PFe : PAl (mol : mol) average SD	DFe : PFe (mol : mol) average SD	n
Iberian Margin	2 and 4	0.07 ± 0.03	0.20 ± 0.01	0.13 ± 0.09	10
East Greenland Margin	56 and 53	0.21 ± 0.09	0.30 ± 0.01	0.12 ± 0.03	6
West Greenland Margin	61	0.18 ± 0.02	0.32 ± 0.01	0.14 ± 0.04	3
Newfoundland Margin	78	1.1 ± 0.41	0.31 ± 0.01	0.06 ± 0.02	4

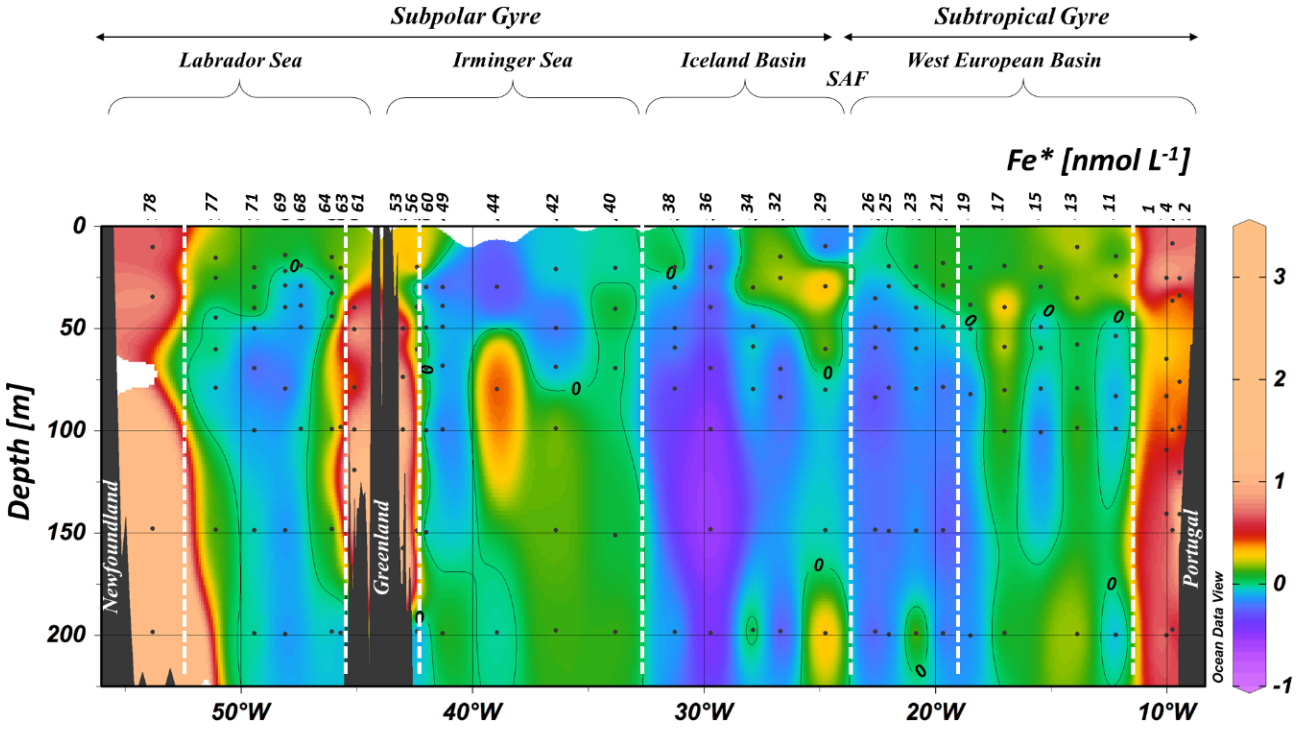

Figure 7. Section plot of the Fe* tracer in the North Atlantic Ocean with a remineralization rate ($R_{Fe:N}$) of 0.05 mmol mol^{-1} from surface to 225 m depth. A contour line of 0 separates areas of negative Fe* from areas with positive Fe*. Positive values of Fe* imply there is enough iron to support complete consumption of NO_3^- when this water is brought to surface, and negative Fe* values imply a deficit. See text for details.

centrations as highlighted by the elevated integrated TChl *a* concentrations ranging from 129.6 (station 78) to 398.3 (station 61) mg m^{-2}. At the Iberian Margin, they likely reflected the influence of the N-limited Tagus River (stations 1, 2, and 4) with its low TChl *a* integrated concentrations that ranged from 31.2 (station 1) to 46.4 (station 4) mg m^{-2}. The high DFe : NO_3^- ratios determined at those stations, which varied from 13.4 (station 78) to 38.6 (station 61) mmol : mol, suggested that waters from these areas, despite having the lowest NO_3^- concentrations, were relatively enriched in DFe compared to waters from the Iceland Basin and the Irminger Sea.

In our study, DFe : NO_3^- ratios displayed a gradient from the West European Basin to Greenland (Figs. S7 and S8). This trend only reverses when the influence of Greenland was encountered, as also observed by Painter et al. (2014). The remineralization of organic matter is a major source of macro- and micronutrients in subsurface waters (from 50 to 250 m depth). Remineralization is associated with the consumption of oxygen, and therefore apparent oxygen utilization (AOU) can provide a quantitative estimate of the amount of material that has been remineralized. While no relationship was observed below 50 m depth for NO_3^- or DFe and AOU considering all the stations, a significant correlation was found in the subpolar gyre when removing the influence of margins (stations 29–49, 56, 60, 63–77) (AOU = 3.36 $NO_3^- - 21.85$, $R^2 = 0.70$, $n = 50$, p value < 0.001). This correlation indicates that remineralization of particulate organic nitrogen (PON) greatly translates into dissolved inorganic nitrogen (DIN) and that NO_3^- can be used as a good tracer for

remineralization in the studied area. Within these subpolar gyre waters, there was a significant correlation between DFe and AOU ($AOU = 23.92\,DFe + 10.45$, $R^2 = 0.37$, $n = 58$, p value < 0.001). The open-ocean stations from the subpolar gyre also exhibited a good linear correlation between DFe and NO_3^- ($DFe = 0.08\,NO_3^- - 0.48$, $R^2 = 0.45$, $n = 50$, p value < 0.05; see Fig. S8). The negative intercept of the regression line reflects possible excess of preformed NO_3^- compared to DFe in these water masses. These significant correlations allow us to use the Fe* tracer to assess where DFe concentrations potentially limit phytoplankton growth by subtracting the contribution of organic matter remineralization from the dissolved Fe pool, as defined by Rijkenberg et al. (2014) and Parekh et al. (2005) for PO_4^{3-} and modified here for NO_3^- as follows:

$$Fe^* = [DFe] - R_{Fe:N} \times \left[NO_3^-\right], \quad (5)$$

where $R_{Fe:N}$ refers to the average biological uptake ratio of Fe over nitrogen, and $[NO_3^-]$ refers to nitrate concentrations in seawater. Although we imposed a fixed biological $R_{Fe:N}$ of 0.05 mmol mol^{-1}, it is important to note that the biological uptake ratio of DFe : NO_3^- is not likely to be constant. Indeed, this ratio has been found to range from 0.05 to 0.9 mmol mol^{-1} depending on species (Ho et al., 2003; Sunda and Huntsman, 1995; Twining et al., 2004). The ratio we choose is thus less drastic to assess potential Fe limitation and more representative of the average biological uptake of DFe over NO_3^- calculated for this study (i.e., $R_{Fe:N} = 0.08 \pm 0.01$ mmol mol^{-1}, for subpolar waters). Negative values of Fe* indicate the removal of DFe that is faster than the input through remineralization or external sources and positive values suggest input of DFe from external sources (Fig. 7). Consequently, Fig. 7 shows that phytoplankton communities with very high Fe requirements relative to NO_3^- ($R_{Fe:N} = 0.9$ mmol mol^{-1}) will only be able to grow above continental shelves where there is a high supply of DFe as previously reported by Nielsdóttir et al. (2009) and Painter et al. (2014). All these results corroborate the importance of the Tagus River (Iberian Margin; see Sect. 4.2.1), glacial inputs in the Greenland and Newfoundland margins (see Sect. 4.2.2), and to a lesser extent atmospheric inputs (see Sect. 4.2.3) in supplying Fe with Fe : N ratios higher than the average biological uptake / demand ratio. Figure 7 (see also Figs. S7, S9, S10, and S11) exhibits Fe : N ratios lower than 0.05 mmol mol^{-1}, suggesting that Fe could also limit the low-Fe requirement phytoplankton class ($R_{Fe:N} =$ 0.05 mmol mol^{-1}) within the Iceland Basin and the Irminger and Labrador seas. The Fe deficiency observed in surface waters (> 50 m depth) from the Irminger and Labrador seas might be explained by low atmospheric deposition to IcSPMW and LSW (Shelley et al., 2017). Low atmospheric Fe supply and sub-optimal Fe : N ratios in winter overturned deep water could favor the formation of the high-nutrient, low-chlorophyll (HNLC) conditions. The West European Basin, despite exhibiting some of the highest DFe : NO_3^- ratios within surface waters, displayed one of the strongest Fe depletions from 50 m depth down to the bottom (see Figs. S9 and S10), suggesting that the main source of Fe was coming from dust deposition and/or riverine inputs.

Similar to the West European Basin, the pattern displayed in the surface map of DFe : NO_3^- ratios (Fig. S9) extended to about 50 m depth, after which the trend reversed (Figs. 7 and S7). Below 50 m depth, the Fe* tracer (Fig. 7) was positive in the Irminger Sea and overall negative in the other basins. In the Irminger Sea positive Fe* values were likely the result of the winter entrainment of Fe-rich LSW (see Sect. 4.2.1) coinciding with high remineralized carbon fluxes in this area (station 44; Lemaitre et al., 2018b) (see Sect. 4.2.2). The largest drawdown in DFe : NO_3^- ratios was observed between stations 34 and 38 and was likely due to the intrusion of IcSPMW, with this water mass exhibiting low DFe and high NO_3^- (from 7 to 8 µmol L^{-1}) concentrations. Similarly, SAIW exhibited high NO_3^- concentrations. Both the IcSPMW and the SAIW sourced from the NAC. The NAC as it flows along the coast of North America receives atmospheric depositions from anthropogenic sources (Shelley et al., 2017, 2015) which deliver high N relative to Fe (Jickells and Moore, 2015) and might be responsible for the observed ranges.

5 Conclusions

The DFe concentrations measured during this study were in good agreement with previous studies that spanned the West European Basin. However, within the Irminger Basin the DFe concentrations measured during this study were up to 3 times higher than those measured by Rijkenberg et al. (2014) in deep waters (> 1000 m depth). This is likely explained by the different water masses encountered (i.e., the Polar Intermediate Water, ∼ 2800 m depth) and by a stronger signal of the Iceland Scotland Overflow Water (ISOW) from 1200 to 2300 m depth. This corresponded to the most striking feature of the whole section with DFe concentrations reaching up to 2.5 nmol L^{-1} within ISOW, Denmark Strait Overflow Water (DSOW), and the Labrador Sea Water (LSW), three water masses that are part of the Deep Western Boundary Current, and was likely the result of a lateral advection of particles in the Irminger Sea. However, as these water masses reached the Labrador Sea, lower DFe levels were measured. These differences could be explained by different processes occurring within the benthic nepheloid layers, where DFe was sometimes trapped onto particles due to Mn sediment within the Labrador Sea (Gourain et al., 2019) and sometimes released from the sediment potentially as a result of interactions with dissolved organic matter. Such Fe-binding organic ligands could have also been produced locally due to the intense remineralization rate reported by Lemaitre et al. (2018b) of biogenic particles (Boyd et al.,

2010; Gourain et al., 2019). The LSW exhibited increasing DFe concentrations along its flow path, likely resulting from sediment inputs at the Newfoundland Margin. Although DFe inputs through hydrothermal activity were expected at the slow-spreading Reykjanes Ridge (Baker and German, 2004; German et al., 1994), our data did not provide evidence of this specific source as previously suggested by Achterberg et al. (2018) at $\sim 60^\circ$ N.

In surface waters several sources of DFe were highlighted especially close to land, with riverine inputs from the Tagus River at the Iberian margin (Menzel Barraqueta et al., 2018) and meteoric inputs (including coastal runoff and glacial meltwater) at the Newfoundland and the Greenland margins (Benetti et al., 2016). Substantial sediment input was observed at all margins but with varying intensity. The highest DFe sediment input was located at the Newfoundland margin, while the lowest was observed at the eastern Greenland margin. These differences could be explained by the different nature of particles with the most lithogenic located at the Iberian margin and the most biogenic at the Newfoundland margin (Gourain et al., 2019). Although previous studies (e.g., Jickells et al., 2005; Shelley et al., 2015) reported that atmospheric inputs substantially fertilized surface waters from the West European Basin, in our study, only stations located in the West European and Iceland basins exhibited enhanced SML DFe inventories with lower TTADs. However, these TTADs were about 3 times higher than those reported for Saharan dust inputs, and thus atmospheric deposition appeared to be a minor source of Fe during the sampling period. Finally, there was evidence of convective inputs of the LSW to surface seawater caused by long tip jet events (Piron et al., 2016) that deepened the winter mixed layer down to ~ 1200 m depth (Zunino et al., 2017), in which Fe was in excess of nitrate and therefore Fe was not limiting.

Data availability. All data are available on LEFE CYBER database at: http://www.obs-vlfr.fr/proof/php/geovide/x_datalist_1.php?xxop=geovide&xxcamp=geovide (Perez et al., 2018), and on request from the corresponding authors.

Supplement. All dissolved iron (DFe) data are available in the Supplement S1. The supplement related to this article is available online at: https://doi.org/10.5194/bg-17-917-2020-supplement.

Author contributions. MT, HP, and GS wrote this article with the advice and remarks of all the other co-authors. MG, FDP, and YG accomplished the analyses of dissolved iron with the help of HP. MB and GR provided data and expertise for the meteoric water and sea ice fraction calculation. AG and PT provided data and expertise for particulate iron and nutrient data, respectively. HP, JB, MC, FL, JLMB, LPC, and RS accomplished the sampling during the GEOVIDE cruise. The project was conceived and funded with the help of HP, PL, and GS.

Competing interests. The authors declare that they have no conflict of interest.

Special issue statement. This article is part of the special issue "GEOVIDE, an international GEOTRACES study along the OVIDE section in the North Atlantic and in the Labrador Sea (GA01)". It is not associated with a conference.

Acknowledgements. We are greatly indebted to the master, Gilles Ferrand, the officers, and crew from the N/O *Pourquoi Pas?* for their logistic support during the GEOVIDE voyage. We would like to give a special thanks to Pierre Branellec, Michel Hamon, Catherine Kermabon, Philippe Le Bot, Stéphane Leizour, Olivier Ménage (Laboratoire d'Océanographie Physique et Spatiale), Fabien Pérault, and Emmanuel de Saint Léger (Division Technique de l'INSU, Plouzané, France) for their technical expertise during clean CTD deployments as well as Emilie Grosteffan and Manon Le Goff for the analysis of nutrients. We also wanted to thank the Pôle Spectrométrie Océan (PSO, Plouzané, France) for letting us use the Element XR HR-ICP-MS. Greg Cutter is also greatly appreciated for his help in setting up the new French clean sampling system. Catherine Schmechtig is thanked for the LEFE CYBER database management. This work was supported in logistics by DT-INSU and GENAVIR. Manon Tonnard was supported by a Cotutelle joint PhD scholarship from the Université de Bretagne Occidentale (UBO-IUEM) and the University of Tasmania (UTAS-IMAS).

Financial support. This research has been supported by the French National Research Agency ANR GEOVIDE (grant no. ANR-13-BS06-0014), the RPDOC BITMAP (grant no. ANR-12-PDOC-0025-01), the French National Center for Scientific Research (grant no. CNRS-LEFE-CYBER), the LabexMER (grant no. ANR-10-LABX-19), and Ifremer (Institut français de recherche pour l'exploitation de la mer).

Review statement. This paper was edited by Catherine Jeandel and reviewed by Christian Schlosser and one anonymous referee.

References

Achterberg, E. P., Steigenberger, S., Marsay, C. M., LeMoigne, F. A., Painter, S. C., Baker, A. R., Connelly, D. P., Moore, C. M., Tagliabue, A., and Tanhua, T.: Iron Biogeochemistry in the High Latitude North Atlantic Ocean, Sci. Rep., 8, 1–15, https://doi.org/10.1038/s41598-018-19472-1, 2018.

Aminot, A., and Kerouel, R.: Dosage automatique des nutriments dans les eaux marines, Edn. Quae, 191 pp., 2007.

Annett, A. L., Skiba, M., Henley, S. F., Venables, H. J., Meredith, M. P., Statham, P. J., and Ganeshram, R. S.: Comparative roles of upwelling and glacial iron sources in Ryder Bay, coastal western Antarctic Peninsula, Mar. Chem., 176, 21–33, https://doi.org/10.1016/j.marchem.2015.06.017, 2015.

Armi, L., Hebert, D., Oakey, N., Price, J., Richardson, P. L., Rossby, T., and Ruddick, B.: The history and decay of a Mediterranean salt lens, Nature, 333, 649–651, https://doi.org/10.1038/333649a0, 1988.

Bacon, S., Gould, W. J., and Jia, Y.: Open-ocean convection in the Irminger Sea, Geophys. Res. Lett., 30, 1246, https://doi.org/10.1029/2002GL016271, 2003.

Baker, A. R., Adams, C., Bell, T. G., Jickells, T. D., and Ganzeveld, L.: Estimation of atmospheric nutrient inputs to the Atlantic Ocean from 50° N to 50° S based on large-scale field sampling: Iron and other dust-associated elements, Global Biogeochem. Cy., 27, 755–767, https://doi.org/10.1002/gbc.20062, 2013.

Baker, A. T. and German, C. R.: On the Global Distribution of Hydrothermal vent Fields, in: Mid-Ocean Ridges: Hydrothermal Interactions Between the Lithosphere and Oceans, Geophysical Monograph Series 148, edited by: German, C. R., Lin, J., and Parson, L. M., 245–266, 2004.

Barton, A. D., Greene, C. H., Monger, B. C., and Pershing, A. J.: The Continuous Plankton Recorder survey and the North Atlantic Oscillation: Interannual- to Multidecadal-scale patterns of phytoplankton variability in the North Atlantic Ocean, Prog. Oceanogr., 58, 337–358, https://doi.org/10.1016/j.pocean.2003.08.012, 2003.

Batchelli, S., Muller, F. L. L., Chang, K. C., and Lee, C. L.: Evidence for Strong but Dynamic Iron-Humic Colloidal Associations in Humic-Rich Coastal Waters, Environ. Sci. Technol., 44, 8485–8490, https://doi.org/10.1021/es101081c, 2010.

Benetti, M., Reverdin, G., Pierre, C., Khatiwala, S., Tournadre, B., Olafsdottir, S., and Naamar, A.: Variability of sea ice melt and meteoric water input in the surface Labrador Current off Newfoundland, J. Geophys. Res.-Ocean., 121, 2841–2855, https://doi.org/10.1002/2015JC011302, 2016.

Benetti, M., Reverdin, G., Lique, C., Yashayaev, I., Holliday, N. P., Tynan, E., Torres-Valdes, S., Lherminier, P., Tréguer, P., and Sarthou, G.: Composition of freshwater in the spring of 2014 on the southern Labrador shelf and slope, J. Geophys. Res.-Ocean., 122, 1102–1121, 10.1002/2016jc012244, 2017.

Bergquist, B. A. and Boyle, E. A.: Dissolved iron in the tropical and subtropical Atlantic Ocean, Global Biogeochem. Cy., 20, GB1015, https://doi.org/10.1029/2005GB002505, 2006.

Bersch, M., Yashayaev, I., and Koltermann, K. P.: Recent changes of the thermohaline circulation in the subpolar North Atlantic, Ocean Dynam., 57, 223–235, https://doi.org/10.1007/s10236-007-0104-7, 2007.

Bonnet, S. and Guieu, C.: Dissolution of atmospheric iron in seawater, Geophys. Res. Lett., 31, L03303, https://doi.org/10.1029/2003gl018423, 2004.

Bonnet, S. and Guieu, C.: Atmospheric forcing on the annual iron cycle in the western Mediterranean Sea: A 1-year survey, J. Geophys. Res., 111, C09010, https://doi.org/10.1029/2005jc003213, 2006.

Boyd, P. W. and Ellwood, M. J.: The biogeochemical cycle of iron in the ocean, Nat. Geosci., 3, 675–682, https://doi.org/10.1038/ngeo964, 2010.

Boyd, P. W., Watson, A. J., Law, C. S., Abraham, E. R., Trull, T., Murdoch, R., Bakker, D. C. E., Bowie, A. R., Buesseler, K. O., Chang, H., Charette, M., Croot, P., Downing, K., Frew, R., Gall, M., Hadfield, M., Hall, J., Harvey, M., Jameson, G., LaRoche, J., Liddicoat, M., Ling, R., Maldonado, M. T., McKay, R. M., Nodder, S., Pickmere, S., Pridmore, R., Rintoul, S., Safi, K., Sutton, P., Strzepek, R., Tanneberger, K., Turner, S., Waite, A., and Zeldis, J.: A mesoscale phytoplankton bloom in the polar Southern Ocean stimulated by iron fertilization, Nature, 407, 695–702, https://doi.org/10.1038/35037500, 2000.

Boyd, P. W., Ibisanmi, E., Sander, S. G., Hunter, K. A., and Jackson, G. A.: Remineralization of upper ocean particles: Implications for iron biogeochemistry, Limnol. Oceanogr., 55, 1271–1288, https://doi.org/10.4319/lo.2010.55.3.1271, 2010.

Buck, C. S., Landing, W. M., Resing, J. A., and Measures, C. I.: The solubility and deposition of aerosol Fe and other trace elements in the North Atlantic Ocean: Observations from the A16N CLIVAR / CO_2 repeat hydrography section, Mar. Chem., 120, 57–70, https://doi.org/10.1016/j.marchem.2008.08.003, 2010.

Canário, J., Vale, C., Caetano, M., and Madureira, M. J.: Mercury in contaminated sediments and pore waters enriched in sulphate (Tagus Estuary, Portugal), Environ. Pollut., 126, 425–433, https://doi.org/10.1016/S0269-7491(03)00234-3, 2003.

Charette, M. A., Morris, P. J., Henderson, P. B., and Moore, W. S.: Radium isotope distributions during the US GEOTRACES North Atlantic cruises, Mar. Chem., 177, 184–195, https://doi.org/10.1016/j.marchem.2015.01.001, 2015.

Chen, Y. J.: Influence of the Iceland mantle plume on crustal accretion at the inflated Reykjanes Ridge: Magma lens and low hydrothermal activity, J. Geophys. Res., 108, 2524, https://doi.org/10.1029/2001JB000816, 2003.

Chester, R., Murphy, K. J. T., Lin, F. J., Berry, A. S., Bradshaw, G. A., and Corcoran, P. A.: Factors controlling the solubilities of trace-metals from nonremote aerosols deposited to the sea-surface by the dry deposition mode, Mar. Chem., 42, 107–126, https://doi.org/10.1016/0304-4203(93)90241-f, 1993.

Conway, T. M. and John, S. G.: Quantification of dissolved iron sources to the North Atlantic Ocean, Nature, 511, 212–215, https://doi.org/10.1038/nature13482, 2014.

Cooper, L. W., Whitledge, T. E., Grebmeier, J. M., and Weingartner, T.: The nutrient, salinity, and stable oxygen isotope composition of Bering and Chukchi Seas waters in and near the Bering Strait, J. Geophys. Res., 102, 12563–512573, 1997.

Cooper, L. W., McClelland, J. W., Holmes, R. M., Raymond, P. A., Gibson, J. J., Guay, C. K., and Peterson, B. J.: Flow-weighted values of runoff tracers (δ^{18}O, DOC, Ba, alkalinity) from the six largest Arctic rivers, Geophys. Res. Lett., 35, 1–5, https://doi.org/10.1029/2008GL035007, 2008.

Crane, K., Johnson, L., Appelgate, B., Nishimura, C., Buck, R., Jones, C., Vogt, P., and Kos'yan, R.: Volcanic and Seismic Swarm Events on the Reykjanes Ridge and Their Similarities to Events on Iceland: Results of a Rapid Response Mission, Mar. Geophys. Res., 19, 319–338, https://doi.org/10.1023/A:1004298425881

Croot, P. L., Streu, P., and Baker, A. R.: Short residence time for iron in surface seawater impacted by atmospheric dry deposition from Saharan dust events, Geophys. Res. Lett., 31, L23S08, https://doi.org/10.1029/2004GL020153, 2004.

Cutter, G., Casciotti, K., Croot, P., Geibert, W., Heimburger, L. E., Lohan, M., Planquette, H., and van de Flierdt, T.: Sampling and the Sample-handling Protocols for GEOTRACES Cruises, 1–178, 2017.

Daniault, N., Mercier, H., Lherminier, P., Sarafanov, A., Falina, A., Zunino, P., Pérez, F. F., Ríos, A. F., Ferron, B., Huck, T., Thierry,

V., and Gladyshev, S.: The northern North Atlantic Ocean mean circulation in the early 21st century, Prog. Oceanogr., 146, 142–158, https://doi.org/10.1016/j.pocean.2016.06.007, 2016.

de Baar, H. J. W. and de Jong, J. T. M.: Distributions, Sources and Sinks of Iron in Seawater, in: Biogeochemistry of Fe in Seawater, chap. 5, edited by: Turner D. R. and Hunter, K. A., SCOR-IUPAC series, J Wiley, Baltimore, 123–253, 2001.

de Barros, M. C.: A case study of waste inputs in the Tagus estuary, in: The role of the Oceans as a Waste Disposal Option, edited by: Kullenberg, G., NATO ASI Series; Series C: Mathematical and Physical Sciences, 172, Springer Netherlands, 307–324, 1986.

de Jong, M. F., van Aken, H. M., Våge, K., and Pickart, R. S.: Convective mixing in the central Irminger Sea: 2002–2010, Deep-Sea Res. Pt. I, 63, 36–51, https://doi.org/10.1016/j.dsr.2012.01.003, 2012.

Dehairs, F., Shopova, D., Ober, S., Veth, C., and Goeyens, L.: Particulate barium stocks and oxygen consumption in the Southern Ocean mesopelagic water column during spring and early summer: Relationship with export production, Deep-Sea Res. Pt. II, 44, 497–516, https://doi.org/10.1016/S0967-0645(96)00072-0, 1997.

Fagel, N., Robert, C., and Hilaire-Marcel, C.: Clay mineral signature of the NW Atlantic Boundary Undercurrent, Mar. Geol., 130, 19–28, https://doi.org/10.1016/0025-3227(95)00134-4, 1996.

Fagel, N., Robert, C., Preda, M., and Thorez, J.: Smectite composition as a tracer of deep circulation: the case of the Northern North Atlantic, Mar. Geol., 172, 309–330, https://doi.org/10.1016/S0025-3227(00)00123-7, 2001.

Ferron, B., Kokoszka, F., Mercier, H., Lherminier, P., Huck, T., Rios, A., and Thierry, V.: Variability of the Turbulent Kinetic Energy Dissipation along the A25 Greenland–Portugal Transect Repeated from 2002 to 2012, J. Phys. Oceanogr., 46, 1989–2003, https://doi.org/10.1175/jpo-d-15-0186.1, 2016.

Figueres, G., Martin, J. M., Meybeck, M., and Seyler, P.: A comparative study of mercury contamination in the Tagus estuary (Portugal) and major French estuaries (Gironde, Loire, Rhone), Estuarine, Coast. Shelf Sci., 20, 183–203, https://doi.org/10.1016/0272-7714(85)90037-X, 1985.

Fiuza, A.: Hidrologia e dinamica das aguas costeiras de Portugal, Ph. D., Universidade de Lisboa, Lisboa, Portugal, unpublished, 194 pp., 1984.

Follows, M. and Dutkiewicz, S.: Meteorological modulation of the North Atlantic Spring Bloom, Deep-Sea Res. Pt. II, 49, 321–344, https://doi.org/10.1016/S0967-0645(01)00105-9, 2001.

García-Ibáñez, M. I., Pardo, P. C., Carracedo, L. I., Mercier, H., Lherminier, P., Ríos, A. F., and Pérez, F. F.: Structure, transports and transformations of the water masses in the Atlantic Subpolar Gyre, Prog. Oceanogr., 135, 18–36, https://doi.org/10.1016/j.pocean.2015.03.009, 2015.

García-Ibáñez, M. I., Pérez, F. F., Lherminier, P., Zunino, P., Mercier, H., and Tréguer, P.: Water mass distributions and transports for the 2014 GEOVIDE cruise in the North Atlantic, Biogeosciences, 15, 2075–2090, https://doi.org/10.5194/bg-15-2075-2018, 2018.

Gaudencio, M. J., Guerra, M. T., and Glemarec, M.: Recherches biosedimentaires sur la zone maritime de l'estuaire du Tage, Portugal: donnees sedimentaires preliminaires, in: Estuaries and Coasts: Spatial and Temporal Intercomparisons, edited by: Elliot, M. and Ducrotoy, J. C., Olsen and Olsen, Fredensborg, 11–16, 1991.

German, C. R., Briem, J., Chin, C. S., Danielsen, M., Holland, S., James, R. H., Jonsdottir, A., Ludford, E., Moser, C., Olafsson, J., Palmer, M. R., and Rudnicki, M. D.: Hydrothermal activity on the Reykjanes Ridge: the Steinahóll vent-field at 63°06′ N, Earth Planet. Sc. Lett., 121, 647–654, https://doi.org/10.1016/0012-821X(94)90098-1, 1994.

Gerringa, L. J. A., Blain, S., Laan, P., Sarthou, G., Veldhuis, M. J. W., Brussaard, C. P. D., Viollier, E., and Timmermans, K. R.: Fe-binding dissolved organic ligands near the Kerguelen Archipelago in the Southern Ocean (Indian sector), Deep-Sea Res. Pt. II, 55, 606–621, https://doi.org/10.1016/j.dsr2.2007.12.007, 2008.

Gerringa, L. J. A., Rijkenberg, M. J. A., Schoemann, V., Laan, P., and de Baar, H. J. W.: Organic complexation of iron in the West Atlantic Ocean, Mar. Chem., 177, 434–446, https://doi.org/10.1016/j.marchem.2015.04.007, 2015.

Gerringa, L. J. A., Slagter, H. A., Bown, J., van Haren, H., Laan, P., de Baar, H. J. W., and Rijkenberg, M. J. A.: Dissolved Fe and Fe-binding organic ligands in the Mediterranean Sea – GEOTRACES G04, Mar. Chem., 194, 100–113, https://doi.org/10.1016/j.marchem.2017.05.012, 2017.

Gourain, A., Planquette, H., Cheize, M., Lemaitre, N., Menzel Barraqueta, J.-L., Shelley, R., Lherminier, P., and Sarthou, G.: Inputs and processes affecting the distribution of particulate iron in the North Atlantic along the GEOVIDE (GEOTRACES GA01) section, Biogeosciences, 16, 1563–1582, https://doi.org/10.5194/bg-16-1563-2019, 2019.

Guerzoni, S., Chester, R., Dulac, F., Herut, B., Loye-Pilot, M.-D., Measures, C., Migon, C., Molinaroli, E., Moulin, C., Rossini, P., Saydam, C., Soudine, A., and Ziveri, P.: The role of atmospheric deposition in the biogeochemistry of the Mediterranean Sea, Prog. Oceanogr., 44, 147–190, https://doi.org/10.1016/S0079-6611(99)00024-5, 1999.

Guieu, C., Loÿe-Pilot, M. D., Benyahya, L., and Dufour, A.: Spatial variability of atmospheric fluxes of metals (Al, Fe, Cd, Zn and Pb) and phosphorus over the whole Mediterranean from a one-year monitoring experiment: Biogeochemical implications, Mar. Chem., 120, 164–178, https://doi.org/10.1016/j.marchem.2009.02.004, 2010.

Guieu, C., Aumont, O., Paytan, A., Bopp, L., Law, C. S., Mahowald, N., Achterberg, E. P., Marañón, E., Salihoglu, B., Crise, A., Wagener, T., Herut, B., Desboeufs, K., Kanakidou, M., Olgun, N., Peters, F., Pulido-Villena, E., Tovar-Sanchez, A., and Völker, C.: The significance of the episodic nature of atmospheric deposition to Low Nutrient Low Chlorophyll regions, Global Biogeochem. Cy., 28, 1179–1198, https://doi.org/10.1002/2014gb004852, 2014.

Harrison, W. G., Yngve Børsheim, K., Li, W. K. W., Maillet, G. L., Pepin, P., Sakshaug, E., Skogen, M. D., and Yeats, P. A.: Phytoplankton production and growth regulation in the Subarctic North Atlantic: A comparative study of the Labrador Sea-Labrador/Newfoundland shelves and Barents/Norwegian/Greenland seas and shelves, Prog. Oceanogr., 114, 26–45, https://doi.org/10.1016/j.pocean.2013.05.003, 2013.

Hatta, M., Measures, C. I., Wu, J., Roshan, S., Fitzsimmons, J. N., Sedwick, P., and Morton, P.: An overview of dissolved Fe and Mn distributions during the 2010-2011 US GEOTRACES north

Atlantic cruises: GEOTRACES GA03, Deep-Sea Res. Pt. II, 116, 117–129, https://doi.org/10.1016/j.dsr2.2014.07.005, 2015.

Henson, S. A., Dunne, J. P., and Sarmiento, J. L.: Decadal variability in North Atlantic phytoplankton blooms, J. Geophys. Res., 114, C04013, https://doi.org/10.1029/2008jc005139, 2009.

Ho, T.-Y., Quigg, A., Finkel, Z. V., Milligan, A. J., Wyman, K., Falkowski, P. G., and Morel, F. M. M.: The elemental composition of some marine phytoplankton, J. Phycol., 39, 1145–1159, https://doi.org/10.1111/j.0022-3646.2003.03-090.x, 2003.

Homoky, W. B., Hembury, D. J., Hepburn, L. E., Mills, R. A., Statham, P. J., Fones, G. R., and Palmer, M. R.: Iron and manganese diagenesis in deep sea volcanogenic sediments and the origins of pore water colloids, Geochim. Cosmochim. Ac., 75, 5032–5048, https://doi.org/10.1016/j.gca.2011.06.019, 2011.

Homoky, W. B., John, S. G., Conway, T. M., and Mills, R. A.: Distinct iron isotopic signatures and supply from marine sediment dissolution, Nat. Commun., 4, 2143, https://doi.org/10.1038/ncomms3143, 2013.

Humphreys, M. P., Griffiths, A. M., Achterberg, E. P., Holliday, N. P., Rérolle, V., Menzel Barraqueta, J. L., Couldrey, M. P., Oliver, K. I., Hartman, S. E., and Esposito, M.: Multidecadal accumulation of anthropogenic and remineralized dissolved inorganic carbon along the Extended Ellett Line in the northeast Atlantic Ocean, Global Biogeochem. Cy., 30, 293–310, https://doi.org/10.1002/2015GB005246, 2016.

Janssens, J., Meiners, K. M., Tison, J.-L., Dieckmann, G., Delille, B., and Lannuzel, D.: Incorporation of iron and organic matter into young Antarctic sea ice during its initial growth stages, Elementa, 4, p.000123, https://doi.org/10.12952/journal.elementa.000123, 2016.

Jickells, T. and Moore, C. M.: The importance of atmospheric deposition for ocean productivity, Annu. Rev. Ecol. Evol. Syst., 46, 481–501, https://doi.org/10.1146/annurev-ecolsys-112414-054118, 2015.

Jickells, T. D., An, Z. C., Andersen, K. K., Baker, A. R., Bergametti, G., Brooks, N., Cao, J. J., Boyd, P. W., Duce, R. A., Hunter, K. A., Kawahata, H., Kubilay, N., laRoche, J., Liss, P. S., Mahowald, N., Prospero, J. M., Ridgwell, A. J., Tegen, I., and Torres, R.: Global iron connections between desert dust, ocean biogeochemistry, and climate, Science, 308, 67–71, https://doi.org/10.1126/science.1105959, 2005.

Jones, E. P., Anderson, L. G., and Swift, J. H.: Distribution of Atlantic and Pacific waters in the upper Arctic Ocean: Implications for circulation, Geophys. Res. Lett., 25, 765–768, https://doi.org/10.1029/98GL00464, 1998.

Kan, C. C., Chen, W. H., Wan, M. W., Phatai, P., Wittayakun, J., and Li, K. F.: The preliminary study of iron and manganese removal from groundwater by NaOCl oxidation and MF filtration, Sustain. Environ. Res., 22, 25–30, 2012.

Kanzow, T. and Zenk, W.: Structure and transport of the Iceland Scotland Overflow plume along the Reykjanes Ridge in the Iceland Basin, Deep-Sea Res. Pt. I, 86, 82–93, https://doi.org/10.1016/j.dsr.2013.11.003, 2014

Kara, A. B., Rochford, P. A., and Hurlburt, H. E.: An optimal definition for ocean mixed layer depth, J. Geophys. Res., 105, 16803–816821, https://doi.org/10.1029/2000JC900072, 2000.

Käse, R. H., Girton, J. B. and Sanford, T. B.: Structure and variability of the Denmark Strait Overflow: Model and observations, J. Geophys. Res.-Ocean., 108, C63181, https://doi.org/10.1029/2002JC001548, 2003.

Klunder, M. B., Bauch, D., Laan, P., de Baar, H. J. W., van Heuven, S. M. A. C., and Ober, S.: Dissolved iron in the Arctic shelf seas and surface waters of the Central Arctic Ocean: impact of Arctic river water and ice-melt, J. Geophys. Res., 117, 1–18, https://doi.org/10.1029/2011JC007133, 2012.

Lackschewitz, K. S., Endler, R., Gehrke, B., Wallrabe-Adams, H.-J., and Thiede, J.: Evidence for topography- and current-controlled deposition on the reykjanes Ridge between 59° N and 60° N, Deep-Sea Res. Pt. I, 43, 1683–1711, https://doi.org/10.1016/S0967-0637(96)00090-8, 1996.

Laës, A., Blain, S., Laan, P., Achterberg, E. P., Sarthou, G., and de Baar, H. J. W.: Deep dissolved iron profiles in the eastern North Atlantic in relation to water masses, Geophys. Res. Lett., 30, 1902, https://doi.org/10.1029/2003gl017902, 2003.

Lagerström, M. E., Field, M. P., Seguret, M., Fischer, L., Hann, S., and Sherrell, R. M.: Automated on-line flow-injection ICP-MS determination of trace metals (Mn, Fe, Co, Ni, Cu and Zn) in open ocean seawater: Application to the GEOTRACES program, Mar. Chem., 155, 71–80, https://doi.org/10.1016/j.marchem.2013.06.001, 2013.

Lambelet, M., van de Flierdt, T., Crocket, K., Rehkamper, M., Katharina, K., Coles, B., Rijkenberg, M. J. A., Gerringa, L. J. A., de Baar, H. J. W., and Steinfeldt, R.: Neodymium isotopic composition and concentration in the western North Atlantic Ocean: Results from the GEOTRACES GA02 section, Geochim. Cosmochim. Ac., 177, 1–29, https://doi.org/10.1016/j.gca.2015.12.019, 2016.

Le Roy, E., Sanial, V., Charette, M. A., van Beek, P., Lacan, F., Jacquet, S. H. M., Henderson, P. B., Souhaut, M., García-Ibáñez, M. I., Jeandel, C., Pérez, F. F., and Sarthou, G.: The ^{226}Ra–Ba relationship in the North Atlantic during GEOTRACES-GA01, Biogeosciences, 15, 3027–3048, https://doi.org/10.5194/bg-15-3027-2018, 2018.

Lemaitre, N., Planchon, F., Planquette, H., Dehairs, F., Fonseca-Batista, D., Roukaerts, A., Deman, F., Tang, Y., Mariez, C., and Sarthou, G.: High variability of particulate organic carbon export along the North Atlantic GEOTRACES section GA01 as deduced from ^{234}Th fluxes, Biogeosciences, 15, 6417–6437, https://doi.org/10.5194/bg-15-6417-2018, 2018a.

Lemaitre, N., Planquette, H., Planchon, F., Sarthou, G., Jacquet, S., García-Ibáñez, M. I., Gourain, A., Cheize, M., Monin, L., André, L., Laha, P., Terryn, H., and Dehairs, F.: Particulate barium tracing of significant mesopelagic carbon remineralisation in the North Atlantic, Biogeosciences, 15, 2289–2307, https://doi.org/10.5194/bg-15-2289-2018, 2018b.

Lohan, M. C. and Bruland, K. W.: Elevated Fe(II) and Dissolved Fe in Hypoxic Shelf Waters off Oregon and Washington: An Enhanced Source of Iron to Coastal Upwelling Regimes, Environ. Sci. Technol., 42, 6462–6468, https://doi.org/10.1021/es800144j, 2008.

Longhurst, A. R.: Ecological geography of the Sea, Second Edition ed., Elsevier Academic Press publications, Burlington, 542 pp., 2007.

Louanchi, F. and Najjar, R. G.: Annual cycles of nutrients and oxygen in the upper layers of the North Atlantic Ocean, Deep-Sea Res. Pt. II, 48, 2155–2171, https://doi.org/10.1016/S0967-0645(00)00185-5, 2001.

Magaldi, M. G., Haine, T. W. N., and Pickart, R. S.: On the Nature and Variability of the East Greenland Spill Jet: A Case Study in Summer 2003, J. Phys. Oceanogr., 41, 2307–2327, https://doi.org/10.1175/JPO-D-10-05004.1, 2011.

Markus, T., Stroeve, J. C., and Miller, J.: Recent changes in Arctic sea ice melt onset, freezeup, and melt season length, J. Geophys. Res., 114, C12024, https://doi.org/10.1029/2009jc005436, 2009.

Marshall, J. and Schott, F.: Open-ocean convection: observations, theory, and models, Rev. Geophys., 37, 1–64, https://doi.org/10.1029/98RG02739, 1999.

Martin, J. D. and Fitzwater, S. E.: Iron deficiency limits phytoplankton growth in the north-east Pacific subarctic, Nature, 331, 341–343, 1988.

Martin, J. H., Fitzwater, S. E., and Gordon, R. M.: Iron deficiencies limits phytoplankton growth in Antarctic waters, Global Biogeochem. Cy., 4, 5–12, https://doi.org/10.1029/GB004i001p00005, 1990.

Martin, J. H., Coale, K. H., Johnson, K. S., Fitzwater, S. E., Gordon, R. M., Tanner, S. J., Hunter, C. N., Elrod, V. A., Nowicki, J. L., Coley, T. L., Barber, R. T., Lindley, S., Watson, A. J., Van Scoy, K., Law, C. S., Liddicoat, M. I., Ling, R., Stanton, T., Stockel, J., Collins, C., Anderson, A., Bidigare, R., Ondrusek, M., Latasa, M., Millero, F. J., Lee, K., Yao, W., Zhang, J. Z., Friederich, G., Sakamoto, C., Chavez, F., Buck, K., Kolber, Z., Greene, R., Falkowski, P., Chisholm, S. W., Hoge, F., Swift, R., Yungel, J., Turner, S., Nightingale, P., Hatton, A., Liss, P., and Tindale, N. W.: Testing the Iron Hypothesis in Ecosystems of the Equatorial Pacific Ocean, Nature, 371, 123–129, https://doi.org/10.1038/371123a0, 1994.

Martin, J.-M., Elbaz-Poulichet, F., Guieu, C., Loÿe-Pilot, M.-D., and Han, G.: River versus atmospheric input of material to the Mediterranean Sea: an overview, Mar. Chem., 28, 159–182, https://doi.org/10.1016/0304-4203(89)90193-X, 1989.

Measures, C. I., Brown, M. T., Selph, K. E., Apprill, A., Zhou, M., Hatta, M., and Hiscock, W. T.: The influence of shelf processes in delivering dissolved iron to the HNLC waters of the Drake Passage, Antarctica, Deep-Sea Res. Pt. II, 90, 77–88, https://doi.org/10.1016/j.dsr2.2012.11.004, 2013.

Melling, H. and Moore, R. M.: Modification of halocline source waters during freezing on the Beaufort Sea shelf: Evidence from oxygen isotopes and dissolved nutrients, Cont. Shelf Res., 15, 89–113, https://doi.org/10.1016/0278-4343(94)P1814-R, 1995.

Menzel Barraqueta, J.-L., Schlosser, C., Planquette, H., Gourain, A., Cheize, M., Boutorh, J., Shelley, R., Contreira Pereira, L., Gledhill, M., Hopwood, M. J., Lacan, F., Lherminier, P., Sarthou, G., and Achterberg, E. P.: Aluminium in the North Atlantic Ocean and the Labrador Sea (GEOTRACES GA01 section): roles of continental inputs and biogenic particle removal, Biogeosciences, 15, 5271–5286, https://doi.org/10.5194/bg-15-5271-2018, 2018.

Mercier, H., Lherminier, P., Sarafanov, A., Gaillard, F., Daniault, N., Desbruyères, D., Falina, A., Ferron, B., Gourcuff, C., Huck, T., and Thierry, V.: Variability of the meridional overturning circulation at the Greenland–Portugal OVIDE section from 1993 to 2010, Prog. Oceanogr., 132, 250–261, https://doi.org/10.1016/j.pocean.2013.11.001, 2015.

Mil-Homens, M., Branco, V., Lopes, C., Vale, C., Abrantes, F., Boer, W., and Vicente, M.: Using factor analysis to charactierise historical trends of trace metal contamination in a sediment core from the Tagus Prodelta, Portugal, Water Air Soil Poll., 197, 277–287, https://doi.org/10.1007/s11270-008-9810-0, 2009.

Moore, C. M., Mills, M. M., Langlois, R., Milne, A., Achterberg, E. P., La Roche, J., and Geider, R. J.: Relative influence of nitrogen and phosphorus availability on phytoplankton physiology and productivity in the oligotrophic subtropical North Atlantic Ocean, Limnol. Oceanogr., 53, 291–205, https://doi.org/10.4319/lo.2008.53.1.0291, 2008.

Moore, C. M., Mills, M. M., Arrigo, K. R., Berman-Frank, I., Bopp, L., Boyd, P. W., Galbraith, E. D., Geider, R. J., Guieu, C., Jaccard, S. L., Jickells, T. D., La Roche, J., Lenton, T. M., Mahowald, N. M., Marañón, E., Marinov, I., Moore, J. K., Nakatsuka, T., Oschlies, A., Saito, M. A., Thingstad, T. F., Tsuda, A., and Ulloa, O.: Processes and patterns of oceanic nutrient limitation, Nat. Geosci., 6, 701–710, https://doi.org/10.1038/ngeo1765, 2013.

Moore, G. W. K.: Gale force winds over the Irminger Sea to the east of Cape Farewell, Greenland, Geophys. Res. Lett., 30, 1894, https://doi.org/10.1029/2003gl018012, 2003.

Morel, F. M. M., Kustka, A. B., and Shaked, Y.: The role of unchelated Fe in the iron nutrition of phytoplankton, Limnol. Oceanogr., 53, 400–404, 2008.

Nielsdóttir, M. C., Moore, C. M., Sanders, R., Hinz, D. J., and Achterberg, E. P.: Iron limitation of the postbloom phytoplankton communities in the Iceland Basin, Global Biogeochem. Cy., 23, GB3001, https://doi.org/10.1029/2008GB003410, 2009.

Olaffson, J., Thors, K., and Cann, J. R.: A sudden cruise off Iceland, RIDGE Events, 2, 35–28, 1991.

Oschlies, A.: Nutrient supply to the surface waters of the North Atlantic: A model study, J. Geophys. Res., 107, 3046, https://doi.org/10.1029/2000jc000275, 2002.

Painter, S. C., Henson, S. A., Forryan, A., Steigenberger, S., Klar, J., Stinchcombe, M. C., Rogan, N., Baker, A. R., Achterberg, E. P., and Moore, C. M.: An assessment of the vertical diffusive flux of iron and other nutrients to the surface waters of the subpolar North Atlantic Ocean, Biogeosciences, 11, 2113–2130, https://doi.org/10.5194/bg-11-2113-2014, 2014.

Palmer, M. R., Ludford, E. M., German, C. R., and Lilley, M. D.: Dissolved methane and hydrogen in the Steinahóll hydrothermal plume, 63° N, Reykjanes Ridge, in: Hydrothermal Vents and Processes, edited by: Parson, L. M., Walker, C. L., and Dixon, D. R., Special Publications, Geological Society, London, 111–120, 1995.

Parekh, P., Follows, M. J., and Boyle, E. A.: Decoupling of iron and phosphate in the global ocean, Global Biogeochem. Cy., 19, GB2020, https://doi.org/10.1029/2004GB002280, 2005.

Parra, M., Delmont, P., Ferragne, A., Latouche, C., Pons, J. C., and Puechmaille, C.: Origin and evolution of smectites in recent marine sediments of the NE Atlantic, Clay Miner., 20, 335–346, https://doi.org/10.1180/claymin.1985.020.3.06, 1985.

Pérez, F. F., Mercier, H., Vázquez-Rodríguez, M., Lherminier, P., Velo, A., Pardo, P. C., Rosón, G., and Ríos, A. F.: Atlantic Ocean CO_2 uptake reduced by weakening of the meridional overturning circulation, Nat. Geosci., 6, 146–152, https://doi.org/10.1038/ngeo1680, 2013.

Pérez, F. F., Treguer, P., Branellec, P., García-Ibáñez, M. I., Lherminier, P., and Sarthou, G.: The 2014 Greenland-Portugal GEOVIDE bottle data (GO-SHIP A25 and GEOTRACES GA01), SEANOE, https://doi.org/10.17882/54653, 2018.

Petrich, C. and Eicken, H.: Growth, structure and properties of sea ice, in: Sea Ice, 2nd Edn., edited by: Thomas, D. N. and Dieckmann, G. S., Wiley-Blackwell, Oxford, UK, 23–77, 2010.

Pickart, R. S., Straneo, F., and Moore, G. W. K.: Is Labrador Sea Water formed in the Irminger basin?, Deep-Sea Res. Pt. I, 50, 23–52, https://doi.org/10.1016/S0967-0637(02)00134-6, 2003.

Piron, A., Thierry, V., Mercier, H., and Caniaux, G.: Argo float observations of basin-scale deep convection in the Irminger sea during winter 2011–2012, Deep-Sea Res. Pt. I, 109, 76–90, https://doi.org/10.1016/j.dsr.2015.12.012, 2016.

R Development Core Team: R: A Language and Environment for Statistical Computing. Vienna. R foundation for Statistical Computing. available at: http://www.R-project.org/ (last access: 18 February 2020), 2012.

Radic, A., Lacan, F., and Murray, J. W.: Iron isotopes in the seawater of the equatorial Pacific Ocean: New constraints for the oceanic iron cycle, Earth Planet. Sc. Lett., 306, 1–10, https://doi.org/10.1016/j.epsl.2011.03.015, 2011.

Ras, J., Claustre, H., and Uitz, J.: Spatial variability of phytoplankton pigment distribution in the Subtropical South Pacific Ocean: comparison between *in situ* and predicted data, Biogeosciences, 5, 353–369, https://doi.org/10.5194/bg-5-353-2008, 2008.

Riebesell, U., Schloss, I., and Smetacek, V.: Aggregation of algae released from melting sea ice: implications for seeding and sedimentation, Pol. Biol., 11, 239–248, https://doi.org/10.1007/BF00238457, 1991.

Rijkenberg, M. J., Middag, R., Laan, P., Gerringa, L. J., van Aken, H. M., Schoemann, V., de Jong, J. T., and de Baar, H. J.: The distribution of dissolved iron in the West Atlantic Ocean, PLoS One, 9, e101323, https://doi.org/10.1371/journal.pone.0101323, 2014.

Sabine, C. L., Feely, R. A., Gruber, N., Key, R. M., Lee, K., Bullister, J. L., Wanninkhof, R., Wong, C. S., Wallace, D. W. R., Tilbrook, B., Millero, F. J., Peng, T.-H., Kozyr, A., Ono, T., and Rios, A. F.: The Oceanic sink for anthropogenic CO_2, Science, 305, 367–371, https://doi.org/10.1126/science.1097403, 2004.

Sanders, R., Brown, L., Henson, S., and Lucas, M.: New production in the Irminger Basin during 2002, J. Mar. Sys., 55, 291–310, https://doi.org/10.1016/j.jmarsys.2004.09.002, 2005.

Santos-Echeandia, J., Vale, C., Caetano, M., Pereira, P., and Prego, R.: Effect of tidal flooding on metal distribution in pore waters of marsh sediments and its transport to water column (Tagus estuary, Portugal), Mar. Environ. Res., 70, 358–367, https://doi.org/10.1016/j.marenvres.2010.07.003, 2010.

Sarthou, G. and Jeandel, C.: Seasonal variations of iron concentrations in the Ligurian Sea and iron budget in the Western Mediterranean Sea, Mar. Chem., 74, 115–129, https://doi.org/10.1016/s0304-4203(00)00119-5, 2001.

Sarthou, G., Baker, A. R., Kramer, J., Laan, P., Laës, A., Ussher, S., Achterberg, E. P., de Baar, H. J. W., Timmermans, K. R., and Blain, S.: Influence of atmospheric inputs on the iron distribution in the subtropical North-East Atlantic Ocean, Mar. Chem., 104, 186–202, https://doi.org/10.1016/j.marchem.2006.11.004, 2007.

Sarthou, G., Laan, P., Ussher, S., Kramer, J., Timmermans, K. R., and Blain, S.: Influence of high atmospheric inputs on the iron distribution in the water column of the North Atlantic Ocean, Deep-Sea Res. Pt. I, 50, 1339–1352, 2003.

Sarthou, G., Vincent, D., Christaki, U., Obernosterer, I., Timmermans, K. R., and Brussaard, C. P. D.: The fate of biogenic iron during a phytoplankton bloom induced by natural fertilisation: Impact of copepod grazing, Deep-Sea Res. Pt. II, 55, 734–751, https://doi.org/10.1016/j.dsr2.2007.12.033, 2008.

Sarthou, G., Lherminier, P., Achterberg, E. P., Alonso-Pérez, F., Bucciarelli, E., Boutorh, J., Bouvier, V., Boyle, E. A., Branellec, P., Carracedo, L. I., Casacuberta, N., Castrillejo, M., Cheize, M., Contreira Pereira, L., Cossa, D., Daniault, N., De Saint-Léger, E., Dehairs, F., Deng, F., Desprez de Gésincourt, F., Devesa, J., Foliot, L., Fonseca-Batista, D., Gallinari, M., García-Ibáñez, M. I., Gourain, A., Grossteffan, E., Hamon, M., Heimbürger, L. E., Henderson, G. M., Jeandel, C., Kermabon, C., Lacan, F., Le Bot, P., Le Goff, M., Le Roy, E., Lefèbvre, A., Leizour, S., Lemaitre, N., Masqué, P., Ménage, O., Menzel Barraqueta, J.-L., Mercier, H., Perault, F., Pérez, F. F., Planquette, H. F., Planchon, F., Roukaerts, A., Sanial, V., Sauzède, R., Schmechtig, C., Shelley, R. U., Stewart, G., Sutton, J. N., Tang, Y., Tisnérat-Laborde, N., Tonnard, M., Tréguer, P., van Beek, P., Zurbrick, C. M., and Zunino, P.: Introduction to the French GEOTRACES North Atlantic Transect (GA01): GEOVIDE cruise, Biogeosciences, 15, 7097–7109, https://doi.org/10.5194/bg-15-7097-2018, 2018.

Schlitzer, R.: Ocean Data View, version 4.7.6, available at: http://odv.awi.de (last access: 30 January 2020), 2016.

Schmidt, S. and Reyss, J.-L.: Radium as internal tracer of Mediterranean Outflow Water, J. Geophys. Res., 101, 3589–3596, 1996.

Shelley, R. U., Morton, P. L., and Landing, W. M.: Elemental ratios and enrichment factors in aerosols from the US-GEOTRACES North Atlantic transects, Deep-Sea Res., 116, 262–272, https://doi.org/10.1016/j.dsr2.2014.12.005, 2015.

Shelley, R. U., Roca-Martí, M., Castrillejo, M., Sanial, V., Masqué, P., Landing, W. M., van Beek, P., Planquette, H., and Sarthou, G.: Quantification of trace element atmospheric deposition fluxes to the Atlantic Ocean (>40° N; GEOVIDE, GEOTRACES GA01) during spring 2014, Deep-Sea Res. Pt. I, 119, 34–49, https://doi.org/10.1016/j.dsr.2016.11.010, 2017.

Shelley, R. U., Landing, W. M., Ussher, S. J., Planquette, H., and Sarthou, G.: Regional trends in the fractional solubility of Fe and other metals from North Atlantic aerosols (GEOTRACES cruises GA01 and GA03) following a two-stage leach, Biogeosciences, 15, 2271–2288, https://doi.org/10.5194/bg-15-2271-2018, 2018.

Sinha, M. C., Navin, D. A., MacGregor, L. M., Constable, S., Peirce, C., White, A., Heinson, G., and Inglis, M. A.: Evidence for accumulated melt beneath the slow-spreading Mid-Atlantic Ridge, Philos. T. R. Soc. A, 355, 233–253, https://doi.org/10.1098/rsta.1997.0008, 1997.

Slagter, H. A., Reader, H. E., Rijkenberg, M. J. A., Rutgers van der Loeff, M., de Baar, H. J. W., and Gerringa, L. J. A.: Organic Fe speciation in the Eurasian Basins of the Arctic Ocean and its relation to terrestrial DOM, Mar. Chem., 197, 11–25, https://doi.org/10.1016/j.marchem.2017.10.005, 2017.

Smallwood, J. R. and White, R. S.: Crustal accretion at the Reykjanes Ridge, 61°–62° N, J. Geophys. Res.-Sol. Ea., 103, 5185–5201, https://doi.org/10.1029/97jb03387, 1998.

Statham, P. J., Skidmore, M., and Tranter, M.: Inputs of glacially derived dissolved and colloidal iron to the coastal ocean and implications for primary productivity, Global Biogeochem. Cy., 22, 1–11, https://doi.org/10.1029/2007GB003106, 2008.

Sunda, W. G. and Huntsman, S. A.: Iron uptake and growth limitation in oceanic and coastal phytoplankton, Mar. Chem., 50, 189–206, https://doi.org/10.1016/0304-4203(95)00035-p, 1995.

Sutherland, D. A., Pickart, R. S., Peter Jones, E., Azetsu-Scott, K., Jane Eert, A., and Ólafsson, J.: Freshwater composition of the waters off southeast Greenland and their link to the Arctic Ocean, J. Geophys. Res., 114, C05020, https://doi.org/10.1029/2008jc004808, 2009.

Tagliabue, A., Aumont, O., DeAth, R., Dunne, J. P., Dutkiewicz, S., Galbraith, E., Misumi, K., Moore, J. K., Ridgwell, A., Sherman, E., Stock, C., Vichi, M., Völker, C., and Yool, A.: How well do global ocean biogeochemistry models simulate dissolved iron distributions?, Global Biogeochem. Cy., 30, 149–174, https://doi.org/10.1002/2015GB005289, 2016.

Tanhua, T., Olsson, K. A., and Jeansson, E.: Formation of Denmark Strait overflow water and its hydrochemical composition, J. Marine Syst., 57, 264–288, https://doi.org/10.1016/j.jmarsys.2005.05.003, 2005.

Teng, Z., Huang, J. Y., Fujito, K., and Takizawa, S.: Manganese removal by hollow fiber micro-filter.Membrane separation for drinking water, Euroopean Conference on Desalination and the Environment, Amsterdam, 28 May, 2001.

Thuróczy, C. E., Gerringa, L. J. A., Klunder, M. B., Middag, R., Laan, P., Timmermans, K. R., and de Baar, H. J. W.: Speciation of Fe in the Eastern North Atlantic Ocean, Deep-Sea Res. Pt. I, 57, 1444–1453, https://doi.org/10.1016/j.dsr.2010.08.004, 2010.

Tonnard, M., Donval, A., Lampert, L., Tréguer, P., Bowie, A. R., van der Merwe, P., planquette, H., Claustre, H., Dimier, C., Ras, J., and Sarthou, G.: Phytoplankton assemblages in the North Atlantic Ocean and in the Labrador Sea along the GEOVIDE section (GEOTRACES section GA01) determined by CHEMTAX analysis from HPLC pigment data, Biogeosciences, in preparation, 2020.

Tovar-Sanchez, A., Duarte, C. M., Alonso, J. C., Lacorte, S., Tauler, R., and Galban-Malagon, C.: Impacts of metals and nutrients released from melting multiyear Arctic sea ice, J. Geophys. Res.-Ocean., 115, C05020, https://doi.org/10.1029/2009jc005685, 2010.

Tréguer, P. J. and De La Rocha, C. L.: The world ocean silica cycle, Annu. Rev. Mar. Sci., 5, 477–501, https://doi.org/10.1146/annurev-marine-121211-172346, 2013.

Twining, B. S., Baines, S. B., Fisher, N. S., and Landry, M. R.: Cellular iron contents of plankton during the Southern Ocean Iron Experiment (SOFeX), Deep-Sea Res. Pt. I, 51, 1827–1850, https://doi.org/10.1016/j.dsr.2004.08.007, 2004.

Van Beusekom, J. E. E.: Distribution of aluminium in surface waters of the North Sea: influence of suspended matter, in: Biogeochemistry and Distribution of Suspended Matter in the North Sea and Implications to fisheries Biology, edited by: Kempe, S., Mittleitungen aus dem Geologisch-Paläontologischen Institut der Universität Hamburg, SCOPE/UNEP Sonderband, 117–136, 1988.

Van Heukelem, L. and Thomas, C. S.: Computer-assisted high-performance liquid chromatography method development with applications to the isolation and analysis of phytoplankton pigments, J. Chromatogr. A, 910, 31–49, 2001.

von Appen, W.-J., Koszalka, I. M., Pickart, R. S., Haine, T. W. N., Mastropole, D., Magaldi, M. G., Valdimarsson, H., Girton, J., Jochumsen, K., and Krahmann, G.: The East Greenland Spill Jet as an important component of the Atlantic Meridional Overturning Circulation, Deep-Sea Res. Pt. I, 92, 75–84, https://doi.org/10.1016/j.dsr.2014.06.002, 2014.

Wadhams, P.: Ice in the Ocean, Gordon and Breach Science Publishers, London, UK, 2000.

Wagener, T., Guieu, C., and Leblond, N.: Effects of dust deposition on iron cycle in the surface Mediterranean Sea: results from a mesocosm seeding experiment, Biogeosciences, 7, 3769–3781, https://doi.org/10.5194/bg-7-3769-2010, 2010. .

Woodgate, R. A. and Aagaard, K.: Revising the Bering Strait freshwater flux into the Arctic Ocean, Geophys. Res. Lett., 32, L02602, https://doi.org/10.1029/2004GL021747, 2005.

Wuttig, K., Wagener, T., Bressac, M., Dammshäuser, A., Streu, P., Guieu, C., and Croot, P. L.: Impacts of dust deposition on dissolved trace metal concentrations (Mn, Al and Fe) during a mesocosm experiment, Biogeosciences, 10, 2583–2600, https://doi.org/10.5194/bg-10-2583-2013, 2013.

Yashayaev, I., Bersch, M., and Aken, H. M. van: Spreading of the Labrador Sea Water to the Irminger and Iceland basins, Geophys. Res. Lett., 34, L10602, https://doi.org/10.1029/2006GL028999, 2007.

Zou, S., Lozier, S., Zenk, W., Bower, A., and Johns, W.: Observed and modeled pathways of the Iceland Scotland Overflow Water in the eastern North Atlantic, Prog. Oceanogr., 159, 211–222, https://doi.org/10.1016/j.pocean.2017.10.003, 2017.

Zunino, P., Lherminier, P., Mercier, H., Daniault, N., García-Ibáñez, M. I., and Pérez, F. F.: The GEOVIDE cruise in May–June 2014 reveals an intense Meridional Overturning Circulation over a cold and fresh subpolar North Atlantic, Biogeosciences, 14, 5323–5342, https://doi.org/10.5194/bg-14-5323-2017, 2017.